

Discovery of A Starburst in the Early Milky Way at $[\text{Fe}/\text{H}] < -2$

BOQUAN CHEN ^{1,2} MATTHEW ORKNEY ^{3,4} YUAN-SEN TING ^{1,2} AND MICHAEL HAYDEN ⁵

¹*Department of Astronomy, The Ohio State University, Columbus, OH 43210, USA*

²*Center for Cosmology and AstroParticle Physics (CCAPP), 191 West Woodruff Avenue, Columbus, OH 43210, USA*

³*Institut de Ciències del Cosmos (ICCUB), Universitat de Barcelona (IEEC-UB), Martí i Franquès 1, E08028 Barcelona, Spain*

⁴*Institut d'Estudis Espacials de Catalunya (IEEC), E-08034 Barcelona, Spain*

⁵*Department of Physics and Astronomy, The University of Oklahoma, 440 W. Brooks St., Norman, OK 73019, USA*

ABSTRACT

We present an analysis of very metal-poor (VMP) and metal-poor stars ($-3.0 < \text{Fe}/\text{H} < -1.5$) in the Gaia BP/RP or XP catalog, which reveals two distinct metallicity distribution functions (MDFs) in regions of the Galactic disk above and below $|z| = 1.0$ kpc. The low- $|z|$ regions display a metallicity peak around $[\text{Fe}/\text{H}] = -2.0$ with a sharp transition in Galactocentric azimuthal velocity (v_ϕ), a feature notably absent in high- $|z|$ regions. Using a galactic chemical evolution (GCE) model, we found that the proto-Milky Way underwent two distinct formation scenarios: a rapid star formation burst followed by quenching near the Galactic center and an extended period of steady star formation. This starburst could have been triggered by a gas-rich accretion event in the first Gyr of our Galaxy's history. Comparison with Milky Way-analog galaxies in Auriga simulations shows strong agreement in the characteristics of this starburst population. During the accretion event, gas rapidly sinks into the inner regions of these analog galaxies, producing the observed MDF peak and the low v_ϕ values. The simulations further indicate that most stars at the metallicity peak formed in situ, rather than through accretion. These findings identify this starburst population as the long-sought in situ component of the proto-Galaxy.

Keywords: keyword1 – keyword2 – keyword3

1. INTRODUCTION

Large-scale spectroscopic surveys (Yanny et al. 2009; De Silva et al. 2015; Majewski et al. 2017; Conroy et al. 2019) and ESA's *Gaia* mission (Perryman et al. 2001; Gaia Collaboration et al. 2023) have gathered a tremendous amount of data, detailing the chemistry and kinematics of the Milky Way across its different regions and formation epochs. The chemo-kinematic data are fundamental to understanding the formation and evolution of our Galaxy through Galactic archaeology (Freeman & Bland-Hawthorn 2002). The epoch immediately succeeding the birth of the Milky Way, referred to as the prototype phase, laid the foundation for the subsequent formation of the thick and thin disk of our Galaxy. Determining the proto-Galaxy's nature would help trace

the evolution pathway to the current Milky Way and potentially locate its counterparts at high redshift.

Recently, several studies have shed light on the period when the Milky Way transitioned from a chaotic, dynamically hot prototype to a rotationally dominated disk galaxy. Conroy et al. (2022) found from the H3 survey that the declining trend of $[\text{Mg}/\text{Fe}]$ caused by the nucleosynthesis of Type Ia supernovae (SNe Ia) was briefly interrupted for around one Gyr before the disk formed thirteen Gyr ago, which could be explained by a sudden increase in the Galactic star formation rate. The orbits of the stars that formed after this unexpected chemical trend became more disk-like. Chen et al. (2024) identified a substantial high-alpha inflow as the cause for the change in $[\text{Mg}/\text{Fe}]$ and the star formation behavior. Belokurov & Kravtsov (2022) quantified this rapid transitional period with data from the APOGEE survey and Gaia mission and proposed a change in the gas accretion mode as the source of angular momentum responsible for “spinning up” the Milky Way. Rix et al. (2022)

searched for Galactic metal-poor stars ($[\text{Fe}/\text{H}] < -1.3$) using the Gaia BP/RP spectra (or “XP” spectra) (Gaia Collaboration et al. 2023). They found a concentration of metal-poor stars in the inner Galactic region, many of which likely formed during the proto-Galaxy phase and are on low-eccentricity orbits indicative of their in situ origin. Chandra et al. (2024) extended the search to a larger sample with additional $[\alpha/\text{Fe}]$ and kinematics from the Gaia mission. They highlighted the role that a massive gas-rich merger, such as the Gaia-Sausage-Enceladus (GSE) (Belokurov et al. 2018; Helmi 2020), could have played in initiating the formation of the Milky Way disk at $[\text{Fe}/\text{H}] \approx -1.0$, and presented a Milky Way analog in the TNG50 simulations capable of reproducing the observational signatures.

Although the end of the prototype phase was widely studied, the properties of the proto-Galaxy itself are more elusive. High-resolution galactic simulations presented various scenarios of the proto-Galaxy. For example, Cooper et al. (2010) found that the proto-Galaxy could be dominated by up to five accreted structures between $1 < z < 7$ in N-body simulations, some of which survive to the present day. Santistevan et al. (2020) reported that in FIRE-2 there are about one hundred galaxies with $M_* \geq 10^5 M_\odot$ which coalesced at $z \sim 3-4$ to form the proto-Galaxy. Renaud et al. (2021) showed with VINTERGATAN that several small galaxies of similar masses rapidly combined through major mergers very early on ($z > 3$). More recently, Horta et al. (2024) revealed that most Milky Way analogs in FIRE-2 originate from one dominant progenitor or two dominant progenitors with similar masses, while less massive components make up the rest of the mass. Despite the evidence for a composite nature of the proto-Galaxy, discerning the individual components could be a difficult task, even with chemo-kinematic data (Kruijssen et al. 2019; Renaud et al. 2021; Brauer et al. 2022). The surviving stars from the proto-Galaxy are also contaminated by mergers at the end of the prototype phase or immediately after, such as the GSE and Kraken/Heracles (Belokurov et al. 2018; Helmi et al. 2018; Naidu et al. 2020; Kruijssen et al. 2020). However, the simulations point to the Galactic center as the least contaminated location for studying the proto-Galaxy once appropriate metallicity cuts are considered (Orkney et al. 2022, 2023).

This study aims to analyze the components of the proto-Galaxy as traced by the metal-poor regime of the metallicity distribution function (MDF), specifically within the range $-3.0 < [\text{Fe}/\text{H}] < -1.5$, which has been lacking in recent literature. The MDF quantifies the stellar density as a function of metallicity and varies depending on both the spatial region and the evolu-

tionary epoch under consideration. Early studies of the MDF focused mainly on the solar neighborhood, which showed an approximate bell shape with a mean metallicity slightly less than the solar value and a long metal-poor tail (van den Bergh 1962; Kobayashi et al. 2006; Schönrich & Binney 2009; Casagrande et al. 2011; Lee et al. 2011; Schlesinger et al. 2012). These earlier studies encompassed a broad range of metallicity values, which tended to obscure detailed features at the metal-poor end of the distribution. Additionally, the proto-Galaxy was much smaller in size, and its signature in the MDF might not extend to the solar neighborhood. Nevertheless, studies of the metal-poor MDF based on limited stellar samples revealed some clues. For example, a bell-shaped metal-poor MDF with a mean $[\text{Fe}/\text{H}] \approx -1.5$ was identified by Hartwick (1976). Subsequent studies found similar MDFs with peaks between $-2.5 < [\text{Fe}/\text{H}] < -1.5$, particularly in the halo and bulge regions, with possible spatial variation in the metal-poor regime (Chiba & Beers 2000; An et al. 2013; Chiti et al. 2021). These findings suggest metal-poor stars hold key insights into the Galaxy’s earliest epoch, though early work often lacked large samples or spatial resolution.

More recently, the APOGEE survey (Majewski et al. 2017) provided the necessary coverage for studying the MDF across the Milky Way disk due to its near-infrared bands, but its sample rapidly depletes as $[\text{Fe}/\text{H}]$ drops below -1.0 . Hayden et al. (2015) showed that the MDF is a function of the distance to the Galactic center (R), the height from the Galactic plane ($|z|$), and whether the sample is restricted to high- or low-alpha stars. The MDF has been subsequently refined to include additional elements and stellar ages (Weinberg et al. 2019; Imig et al. 2023). In theory, the MDF at given (R , $|z|$, age) should largely reflect the star formation and chemical evolution history of stars born in situ, but could be modified by accreted stars and the radial migration of stars from other regions, especially given that stars in the proto-Galaxy are older than ten Gyr (Loebman et al. 2016; Lian et al. 2022; Mori et al. 2024). Although these studies describe the MDF in detail within the metal-rich regime, they lack the metal-poor stars to probe into the earliest epoch of our Galaxy. However, large spectroscopic surveys, including the APOGEE and LAMOST (Zhao et al. 2012), serve as excellent training data for the Gaia XP spectra (Gaia Collaboration et al. 2023). Metallicity and even $[\alpha/\text{Fe}]$ have been derived from these spectra for millions of stars up to 220 million through various machine learning methods (Andrae et al. 2023b,a; Zhang et al. 2023; Xylakis-Dornbusch et al. 2024; Hattori 2024; Khalatyan et al. 2024; Li

et al. 2024; Fallows & Sanders 2024). Despite potentially large errors at low metallicity, these catalogs provide the largest sample and best spatial coverage for studying the metal-poor MDF in our Galaxy.

In this work, we analyze the MDF within $-3.0 < [\text{Fe}/\text{H}] < -1.5$ and discover a prominent metallicity peak at $[\text{Fe}/\text{H}] \approx -2.0$ in the Galactic plane, which we identify as evidence of an ancient starburst that produced over $10^9 M_{\odot}$ of stars about 13 billion years ago. This starburst population is most visible near the Galactic center and disk plane, exhibits slow rotation ($v_{\phi} < 100$ km/s), and its spatial distribution suggests it was shaped by disk heating mechanisms. Our study leverages the unprecedented sample of metal-poor stars now available to reveal this key phase in our Galaxy’s early history.

The organization of this paper is as follows: Section 2 provides an overview of the metallicity catalogs derived from Gaia XP spectra, describes the observational data from which we extract the MDFs for metal-poor stars in the Milky Way, and introduces the bimodal nature of these MDFs observed in our data. Section 3 outlines our GCE framework and presents the models developed to reproduce the observed MDFs. In Section 4, we analyze Milky Way analogs from cosmological simulations and compare their MDF properties to our observational findings. Finally, Section 5 discusses the implications of our results, and Section 6 offers concluding remarks.

2. METALLICITY FROM GAIA XP SPECTRA

The Gaia mission, designed primarily for astrometry, has also been proven to be a powerful spectroscopic tool. Gaia DR3 made public a massive collection of low-resolution BP/RP spectra for over 200 million stars, obtained by combining measurements from the spacecraft’s blue photometer (BP) and red photometer (RP) (Gaia Collaboration et al. 2023). These spectra span a wavelength range of 330-1050 nm. Unlike traditional spectra that provide flux values at specific wavelengths, XP spectra are represented by a set of coefficients that weight a series of basis functions. This representation allows for efficient storage and processing of the vast amount of spectral data collected by Gaia (De Angeli et al. 2023). However, it also presents challenges for traditional spectral analysis techniques that rely on the identification and measurement of individual spectral lines. The signal-to-noise ratio (SNR) can reach ~ 1000 for stars with $9 < G < 12$ but lower than 100 for dimmer stars ($G < 15$).

Despite their low resolution ($R \sim 15-85$), XP spectra have been successfully utilized to estimate fundamental stellar parameters such as effective temperature (T_{eff}),

surface gravity ($\log g$), and metallicity ($[\text{Fe}/\text{H}]$). The broad wavelength coverage and relatively high signal-to-noise ratio of XP spectra enable the identification of subtle features and trends that correlate with these parameters. Furthermore, recent studies have even demonstrated the feasibility of extracting more detailed abundance information, such as alpha-element abundances ($[\alpha/\text{M}]$), from these spectra, pushing the boundaries of what was previously thought possible with such low-resolution data. The availability of XP spectra for a vast number of stars, coupled with the development of innovative data-driven and machine-learning techniques, has opened up new avenues for exploring the properties and evolution of stellar populations across the Milky Way.

2.1. Overview of Gaia XP metallicity catalogs

We will discuss the available Gaia XP metallicity catalogs sorted by their training methods before selecting one for our study. Forward modeling methods generate synthetic data based on a set of assumed model parameters and physical principles. The models are then compared to observed data to assess the model’s validity and refine parameter estimates, providing better interpretability and integrated handling of missing data and systematics. Andrae et al. (2023b) utilize Bayesian inference with PARSEC isochrones and stellar atmosphere models (MARCS, PHOENIX, A-stars, and OB), fitting the observed XP spectra, parallax, and G magnitude to estimate stellar parameters (T_{eff} , $\log g$, $[\text{Fe}/\text{H}]$), distances, and extinctions for 471 million sources. Their model, known as the general symmetric parameterizer from photometry (GSP-Phot), is part of the Gaia DR3 release. They employ an ensemble Markov Chain Monte Carlo (MCMC) sampler to optimize the choice of stellar atmosphere models and predicted parameters for generating the closest matching spectra. Zhang et al. (2023)¹ instead train The Payne (Ting et al. 2019; Xiang et al. 2022) on the atmospheric parameters of LAMOST (covering the main sequence and giant branch stars), parallaxes from Gaia DR3, and reddening from the Bayestar19 dust map by Green et al. (2019) to predict XP spectra. The model is optimized by maximizing the likelihood of the observed spectra and 2MASS/WISE near-infrared photometry (Skrutskie et al. 2006; Meisner et al. 2021) through gradient descent, which yields estimates for 220 million stars.

Discriminative models, in contrast to forward modeling, learn the direct relationship between spectral features and stellar labels from labeled training data, al-

¹ <https://zenodo.org/records/7811871>

lowing them to infer these labels directly from observed spectra. Several recent studies have leveraged this approach to derive stellar metallicities from Gaia XP spectra. For instance, [Xylakis-Dornbusch et al. \(2024\)](#) developed a flux ratio-based empirical method, utilizing specific flux ratios (e.g., Ca H & K lines to the H β region and the G-band to the Ca near-infrared (NIR) triplets) to estimate metallicities for 10 million stars. This method, previously used to identify metal-poor stars ([Xylakis-Dornbusch et al. 2022](#)), was trained on a cross-matched catalog combining Gaia DR3 XP with data from the Stellar Abundances for Galactic Archaeology (SAGA) or the Galactic Archaeology with HERMES (GALAH) surveys. Another study by [Ye et al. \(2024\)](#)² used APOGEE stars to predict flux corrections based on stellar colors, magnitudes, and extinction, applying these corrections to Gaia XP spectra using GaiaXPY³. They then employed Powell’s UOBYQA algorithm to determine atmospheric parameters via a chi-squared fit, resulting in 68 million metallicity estimates and a catalog of 124,188 metal-poor stars with $[\text{Fe}/\text{H}] < -2.5$. Finally, [Andrae et al. \(2023a\)](#)⁴ employed the XGBoost algorithm, a machine learning technique that combines multiple decision trees through gradient boosting, to estimate $[\text{Fe}/\text{H}]$ from Gaia XP spectra. By training their model on a combined dataset from APOGEE DR17 and very metal-poor stars from [Li et al. \(2022\)](#), they expanded the metallicity range beyond what a model trained solely on APOGEE could achieve. Their model incorporates XP spectral coefficients, narrowband and broadband magnitudes (including CatWISE), and parallax to improve accuracy, resulting in a catalog of approximately 175 million stars with metallicity estimates. While the mean precision is 0.1 dex in $[\text{Fe}/\text{H}]$, it decreases for fainter stars ($G \sim 17$).

The decision tree algorithms used by [Andrae et al. \(2023a\)](#) improve upon basic decision trees by sequentially adding new trees that correct the errors of the previous ones, guided by gradient boosting which minimizes the error between the predicted and true $[\text{Fe}/\text{H}]$ values. Decision trees are known for their speed, accuracy, and ability to handle complex data like the Gaia XP spectra and are utilized by several other recent studies. [Hattori \(2024\)](#)⁵ utilizes quantile regression forests (QRFs) which derive the full probability distribution of the target variable, providing not only point estimates

but also uncertainty information, unlike traditional regression forests. The study used the same training set as [Andrae et al. \(2023a\)](#) and reported a root mean square error (RMSE) of 0.0890 dex for $[\text{Fe}/\text{H}]$ and 0.0436 dex for $[\alpha/\text{M}]$ and suggested the potential use of the Na D lines and the Mg I line for inferring $[\alpha/\text{M}]$. [Khalatyan et al. \(2024\)](#)⁶ present SHBoost, a catalog of stellar parameters and extinctions derived from Gaia DR3 XP spectra, astrometry, and multi-wavelength photometry. The authors employ XGBoost regression to train their model on a dataset of roughly 7 million stars with high-quality parameters from the StarHorse catalog, which combines data from various ground-based spectroscopic surveys. This approach enables them to estimate parameters for over 217 million stars, including white dwarfs and hot stars that are often poorly covered by other surveys. Their output includes extinction, T_{eff} , $\log g$, metallicity, and mass estimates, along with reliable uncertainties. In addition, the model offers interpretability through SHapley Additive exPlanations (SHAP) values, allowing insight into the importance of features in the predictions. [Yao et al. \(2024\)](#) identified 200,000 very metal-poor VMP stars with $[\text{Fe}/\text{H}] < -2.0$ from XP spectra, including $\sim 40,000$ faint ones ($\text{BP} > 16$). Their model achieves a recall rate of 93% and a precision rate of 73% on a test set of spectroscopically confirmed VMP stars.

The complex, high-dimensional, and often nonlinear relationship between spectra and stellar labels makes neural networks a popular choice for inferring stellar labels. [Fallows & Sanders \(2024\)](#)⁷ utilize an uncertain neural network (UNN) trained on APOGEE data to predict stellar parameters and abundances, incorporating techniques to estimate both aleatoric and epistemic uncertainties. They implemented dropout during training to prevent overfitting and during training to emulate an ensemble of similarly trained models. An additional layer was added to the design to account for errors and unknown factors in the spectra. Their model reports median formal uncertainties of 0.068 dex, 69.1 K, 0.14 dex, 0.031 dex, 0.040 dex and 0.029 dex for $[\text{Fe}/\text{H}]$, T_{eff} , $\log g$, $[\text{C}/\text{Fe}]$, $[\text{N}/\text{Fe}]$, and $[\alpha/\text{M}]$, respectively. [Kane et al. \(2024\)](#)⁸ utilized a multi-layer perceptron neural network for heteroscedastic regression to predict stellar parameters and abundances and classified 878 stars with globular cluster origins based on $[\text{N}/\text{O}]$ and $[\text{Al}/\text{Fe}]$

² <https://zenodo.org/records/14028589>

³ <https://gaia-dpci.github.io/GaiaXPY-website/>

⁴ <https://zenodo.org/records/7945154>

⁵ <https://zenodo.org/records/10902172>

⁶ <https://data.aip.de/projects/shboost2024.html>

⁷ <https://zenodo.org/records/12660210>

⁸ <https://zenodo.org/records/10469859>

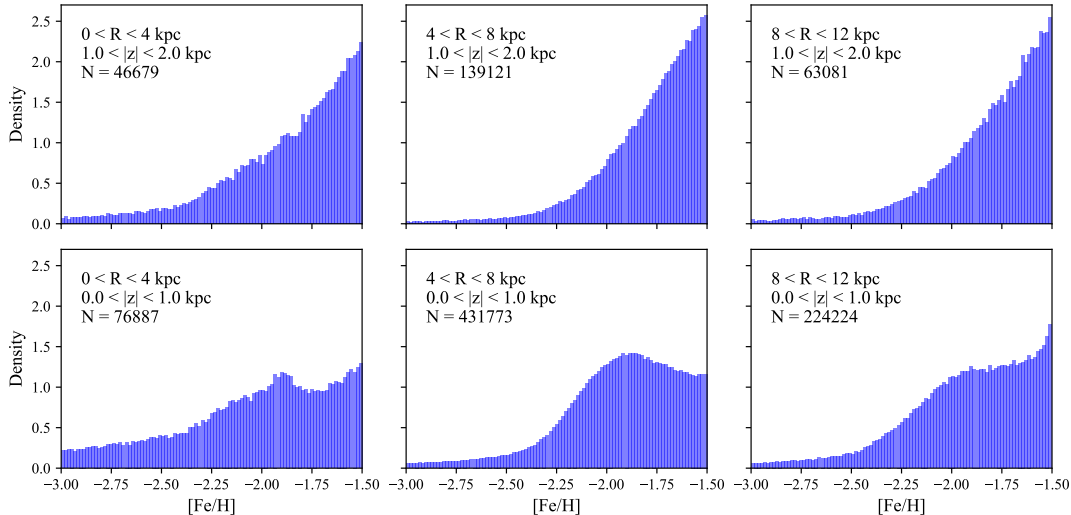


Figure 1. The metal-poor metallicity distribution ($[\text{Fe}/\text{H}] < -1.5$) as a function of the Galactocentric distance (R) and height from the disk plane ($|z|$) in the Milky Way. We adopt the Gaia XP metallicity catalog from Zhang et al. (2023) for better coverage of metal-poor stars. The ranges of R and $|z|$ and the number of the stars within are shown in the top left corner.

abundances. Li et al. (2024)⁹ employed AspGap, a neural network-based model trained on APOGEE spectra and labels, with a “hallucinator” component which generates high-resolution APOGEE-like spectra from the low-resolution Gaia XP spectra. The training dataset is constructed by resampling stars into various $[\text{Fe}/\text{H}]$ - $[\alpha/\text{M}]$ bins to ensure a balanced representation across the abundance space. They claimed an accuracy of 0.03 dex for $[\alpha/\text{M}]$ in giant stars. Laroche & Speagle (2024)¹⁰ employed a unique approach using a scatter variational autoencoder (sVAE), a generative model designed to learn both the underlying structure of XP spectra and the intrinsic scatter or noise present in the data, without the need for labeled training data. The sVAE approach learns from the spectra alone by encoding them into a latent space, capturing both the major patterns and the inherent variability. The authors demonstrate that their model can capture meaningful $[\alpha/\text{M}]$ information directly from the XP spectra, particularly for stars with $T_{\text{eff}} < 5000$ K. In particular, they were able to retrieve the α -bimodality in the data.

The accuracy and applicability of these catalogs derived from XP spectra are influenced by the specific choices made in their training datasets and methodologies, leading to varying limitations in their performance across different stellar populations and parameter regimes. Discriminative models require training data to be well represented in the parameter space and

risk producing systematic biases in the elemental abundances (Ting 2024). However, many metallicity catalogs derived from these models are primarily trained on APOGEE data, which lack sufficient representation of metal-poor stars, such as Hattori (2024); Fallows & Sanders (2024); Kane et al. (2024); Li et al. (2024). Although incorporating additional metal-poor samples, such as the one by Li et al. (2022), can help mitigate this issue, models heavily reliant on APOGEE data may still exhibit biases and selection effects in their predicted metallicities in the metal-poor regime. We selected the metallicity catalog by Zhang et al. (2023) for a few reasons. Their training set leverages the LAMOST survey, which contains more than 10 million stellar spectra and encompasses a diverse range of stellar types and metallicities, including a significant portion of metal-poor stars. Their training method involves developing a data-driven forward model of Gaia XP spectra that can inherently deal with missing or low-quality data. Lastly, their output catalog has substantial coverage with 220 million stars, allowing us to study the metallicity distribution across the Milky Way even at low metallicity.

2.2. The MDF of metal-poor stars in the Milky Way

We used a subset of the catalog from Zhang et al. (2023), selecting stars with metallicities in the range $-3.0 < [\text{Fe}/\text{H}] < -1.5$, $[\text{Fe}/\text{H}]$ confidence > 0.8 , effective temperatures $T_{\text{eff}} < 7000$ K, renormalised unit weight error (RUWE) < 1.4 , and astrometric excess noise (AEN) < 1.0 . This subset comprises 1,439,588 stars. They used a separate pipeline called the “hot Payne” to handle the hot stars based on Xiang et al.

⁹ <https://zenodo.org/records/10469859>

¹⁰ <https://zenodo.org/records/10951393>

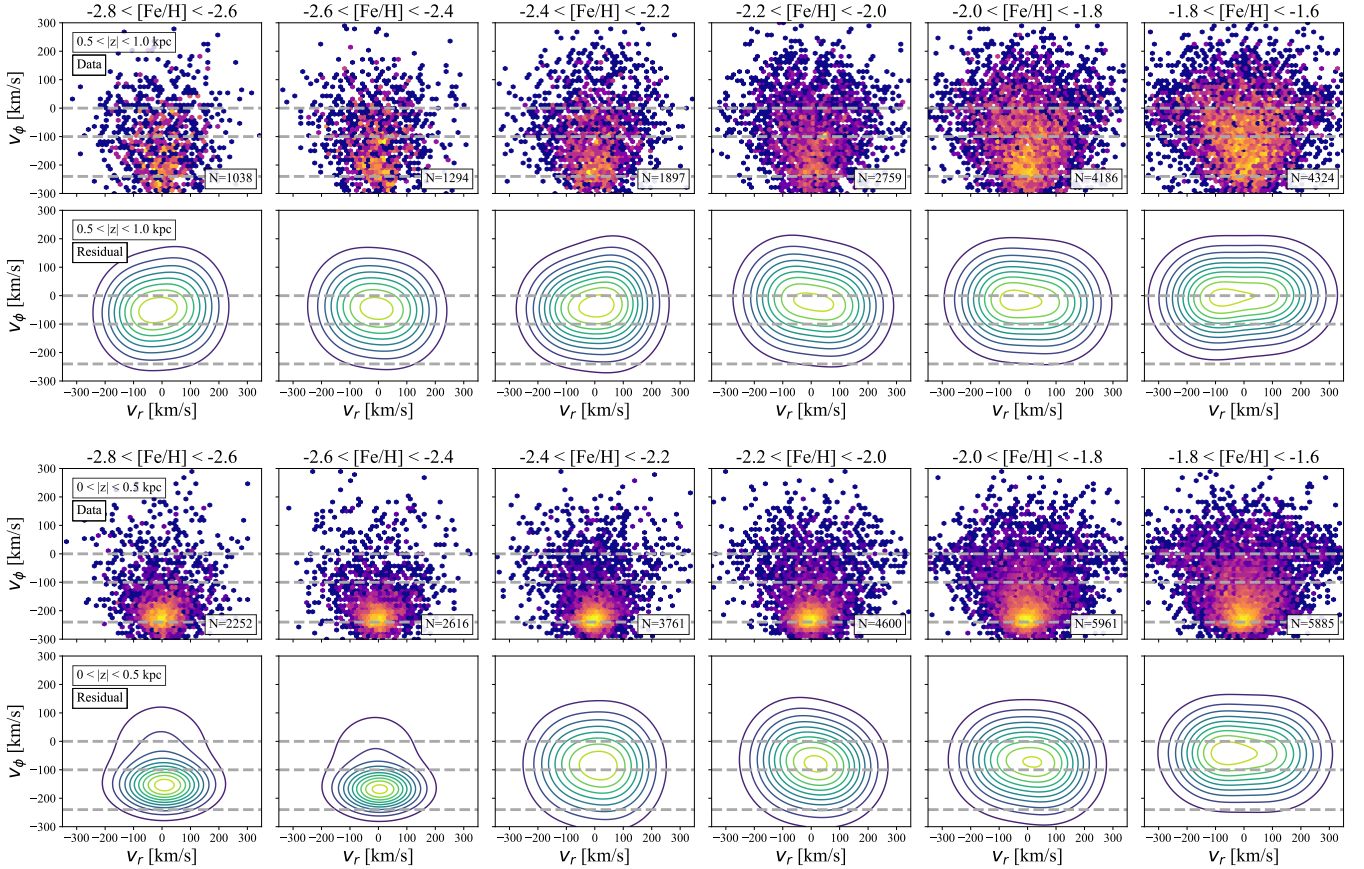


Figure 2. The distribution and GMM residuals of Galactocentric radial and azimuthal velocities for metal-poor stars in Gaia XP and RVS, as a function of $[\text{Fe}/\text{H}]$, for $|z| < 0.5$ kpc and $0.5 < |z| < 1.0$ kpc. The top rows in each $|z|$ panel display the density distribution of velocities in bins of increasing $[\text{Fe}/\text{H}]$. The number of stars satisfying the $|z|$ and $[\text{Fe}/\text{H}]$ selection criteria in each panel is indicated in the bottom-right corner. The bottom rows in each $|z|$ panel show the density distribution of residuals from the GMM fits after subtracting the Gaussian component with the highest weight. Horizontal dashed lines mark three key v_ϕ values: -240 km/s, -100 km/s, and 0 km/s. Most stars have v_r and v_ϕ values associated with the thin disk, but there is a sharp transition in residual v_ϕ when $[\text{Fe}/\text{H}]$ crosses -2.4 at $|z| < 0.5$ kpc.

(2022). By limiting our sample to stars with $T_{\text{eff}} < 7000$ K, we can remove hot stars that are disguised as metal-poor stars in our sample. Their inferred and observed $[\text{Fe}/\text{H}]$ values in the validation set agree with $\sigma_{\text{Fe}/\text{H}} \approx 0.15$. Nevertheless, we restrict our sample to stars with at least 80% confidence in $[\text{Fe}/\text{H}]$. The $[\text{Fe}/\text{H}]$ confidence is a probability ranging between zero and one, which indicates how reliable the stellar parameters, (T_{eff} , $\log(g)$, $[\text{Fe}/\text{H}]$), are. Based on the validation set, their method tends to underestimate the $[\text{Fe}/\text{H}]$ at low metallicity (see their Figure 10) and thus metal-rich stars are unlikely to pass as metal-poor in our sample. The Gaia astrometric solutions (α , δ , ϖ) are converted to Galactocentric distances (R) and heights from the disk plane ($|z|$) with the Astropy package (Astropy Collaboration et al. 2022). Figure 1 shows the metal-poor MDF of this sample in different (R , $|z|$) locations. The range of R and $|z|$ and the number of stars that form the MDF are listed

in the top left corner of each panel. We can observe that the MDF in the low- $|z|$ panels are manifested in a bell shape with a peak around $[\text{Fe}/\text{H}] \approx -2.0$ compared to an ascending exponential shape in high- $|z|$ panels. Other than our catalog, a similar bell-shaped MDF can also be seen in the Pristine Inner Galaxy Survey (PIGS) (see Fig. 6 in Ardern-Arentsen et al. (2024)) but it could be produced due to their selection of metal-poor bulge stars.

2.3. Velocity distribution of metal-poor stars

A cross-match between our Gaia XP catalog and the Gaia RVS leaves 8.3% of the metal-poor stars in our original sample. Figure 2 shows the distribution of the remaining sample in the Galactocentric radial and azimuthal velocity, v_r and v_ϕ , as a function of $[\text{Fe}/\text{H}]$ in two $|z|$ -ranges, $|z| < 0.5$ kpc and $0.5 < |z| < 1.0$ kpc in the top and bottom two rows respectively. The top rows for both $|z|$ -ranges illustrate the raw density dis-

tribution of our cross-matched sample. The majority of stars have v_r and v_ϕ values consistent with the disk orbits with $v_\phi \approx 240$ km/s. This is surprising because we expect most stars in the halo to be non-rotating. One possible explanation is the combined sample bias of the Gaia XP catalog including mostly bright stars ($G > 17.65$) with well-measured spectrum shape coefficients (SSCs) and the RVS. About 80% of the stars in the cross-match reside in the solar neighborhood. However, this could also be related to [Xiang et al. \(2024\)](#) which claims a sizable population with disk-like geometry even thirteen Gyr ago, named *PanGu*.

The Gaia sausage with negligible v_ϕ becomes more visible as $[\text{Fe}/\text{H}]$ surpasses -2.0 . We fitted the (v_r, v_ϕ) -distributions with Gaussian mixture models to reveal the residual velocity when the stars on disk orbits are removed. Based on the Bayesian information criterion (BIC), most velocity density distributions in [Fig. 2](#) are well approximated by two to three components. We chose three components for consistency across the panels. The bottom rows for both $|z|$ -ranges reveal the combined residual velocity distribution at different $[\text{Fe}/\text{H}]$. At $|z| < 0.5$, the residual v_ϕ remains around 200 km/s when $[\text{Fe}/\text{H}]$ is less than -2.4 and lowers to around 100 km/s when above. v_ϕ lowers again when $[\text{Fe}/\text{H}]$ rises above -1.8 when the Gaia sausage becomes prominent. For $0.5 < |z| < 1.0$ kpc, the residual v_ϕ starts at around 50 km/s at low metallicity and lowers to zero as the metallicity climbs. Since the peak metallicity we identified in [Fig. 1](#) is -2.0 , it is possible that the sharp transition in the residual v_ϕ as $[\text{Fe}/\text{H}]$ crosses -2.4 is a signature of the event leading to the peak. This subtle velocity signature quickly fades into the Sausage as metallicity increases. We use three dashed gray lines to indicate three key v_ϕ values, -240 km/s (rotation velocity of the Sun), -100 km/s (possible azimuthal velocity of the starburst population today), and 0 km/s (for the Gaia sausage).

3. CHEMICAL EVOLUTION MODEL

In the last section, we provided a brief overview of the various Gaia XP metallicity catalogs available and explained why we chose the catalog by [Zhang et al. \(2023\)](#) due to its uniform training set, forward modeling technique, and massive output. We found that the MDFs in regions below and above $|z| = 1.0$ kpc are distinct. The cross-match between Gaia XP and RVS revealed that most stars in our metallicity range in the low- $|z|$ have v_ϕ of around 240 km/s, but the residual v_ϕ could be much lower. In this section, we will provide the necessary details of our GCE model used to replicate the MDFs presented in [Fig. 1](#) above (see [Andrews et al. \(2017\)](#)

and [Chen et al. \(2023\)](#) for details) and present the star formation scenarios leading to those MDFs. GCE models are efficient tools to study the evolution of elemental abundances inside galaxies. They reveal the underlying physical processes by matching the observed chemical characteristics.

3.1. Model description

GCE models are theoretical frameworks that simulate the chemical enrichment of galaxies over time. These models track how the abundances of chemical elements evolve within a galaxy, driven by processes such as star formation, stellar evolution, and gas flows. GCE models are employed to extract physical insights from large metallicity catalogs by replicating observed MDF. Since the advent of large-scale spectroscopic surveys, GCE models have become increasingly important tools for studying the physical processes within our Galaxy, particularly the evolution of the disk. They have been applied to reproduce the complex elemental abundance space and chemodynamical behaviors of the Galaxy ([Minchev et al. 2013](#); [Kubryk et al. 2015](#); [Andrews et al. 2017](#); [Spitoni et al. 2019](#); [Lian et al. 2020](#); [Spitoni et al. 2021](#); [Johnson et al. 2021](#); [Chen et al. 2023](#); [Chen & Prantzos 2025](#)), and to estimate nucleosynthesis yields from specific channels ([Prantzos et al. 2018](#); [Ojima et al. 2018](#); [Lian et al. 2023](#)).

The GCE model we adopt has the following ingredients: warm and cold interstellar medium (ISM), stellar mass bins, nucleosynthesis of elements, and inflow and outflow. These ingredients allow elements to form or be introduced to the system within which the elemental abundances are recorded at each time step ($dt = 30$ Myr). Our GCE galaxy is simulated as a flat box with a radius of $R = 1$ kpc.

3.1.1. Warm and cold ISM

The warm and cold ISM are the first ingredients in our model that exist before any star formation activity takes place. We initialize our model with warm and cold ISM whose elemental compositions are pristine (only H, He, and Li) ([Wagoner et al. 1967](#)). The respective initial mass for each ISM is assigned $m_{\text{cold},0}$ and $m_{\text{warm},0}$, both ranging from 10^8 to $10^{10} M_\odot$. The cold ISM is only responsible for forming stars which inherit its elemental composition. The warm ISM stores the elements produced in various nucleosynthesis channels and those introduced through inflow. The warm ISM also cools to the cold ISM exponentially over time as governed by the cooling timescale t_{cool} that ranges from 100 Myr to 10 Gyr based on the results of EAGLE simulations by [Stevens et al. \(2017\)](#). Further, star formation and nucleosynthesis events heat cold ISM several times as mas-

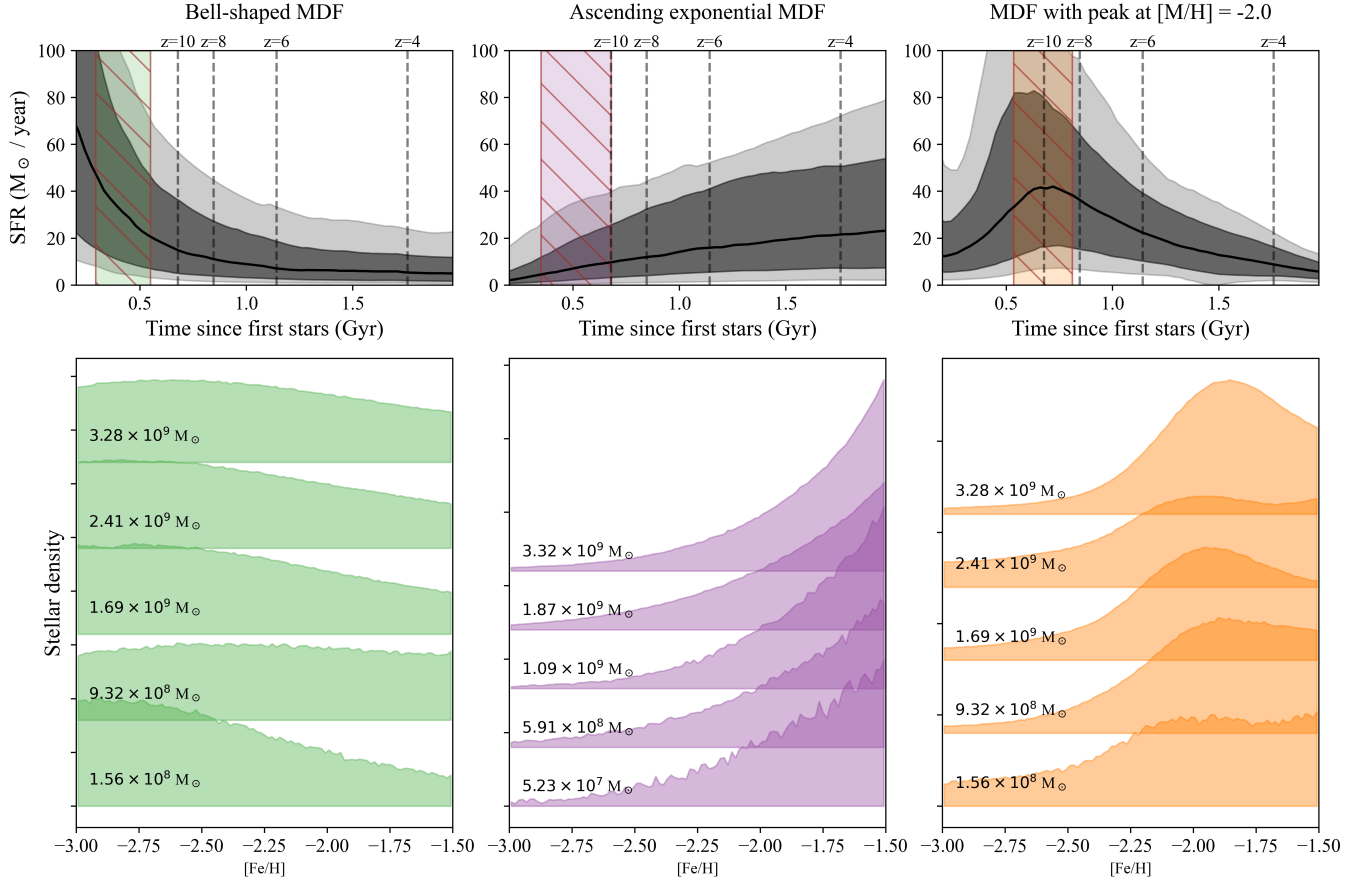


Figure 3. SFHs (top panels) and MDFs (bottom panels) from our GCE models, categorized by MDF morphology. The models reproduce observed bell-shaped, ascending, and $[\text{Fe}/\text{H}] = -2.0$ -peak MDFs. In the top panels, black solid lines show the median SFR, with dark and light gray regions denoting one-sigma and two-sigma spreads, respectively. Vertical shaded bands indicate the time when $[\text{Fe}/\text{H}]$ reaches -2.0 for each MDF category. Key redshifts are marked with vertical dashed lines. The bottom panels present five representative MDFs per category, ranked by the total stellar mass across the range. The total stellar mass corresponding to each MDF is listed on the left. The MDF shape correlates with the SFH of the GCE model that generates it.

sive as the cold ISM involved in them. The mass loading factors that govern the heating processes are called $\eta_{\text{SF}} = 2.0$ and $\eta_{\text{SN}} = 5.0$. These factors can range from one to 100, but typically remain below ten (Schneider & Robertson 2018; Kim et al. 2020).

3.1.2. Stellar mass bins

Cold ISM is converted into stars in the model according to the Kennicutt-Schmidt (K-S) law which relates the surface gas density to star formation rate (SFR), $\Sigma_{\text{SFR}} = \epsilon_{\text{KS}} \Sigma_{\text{gas}}^n$ (Schmidt 1959; Kennicutt 1998). Our ϵ_{KS} ranges between 10^{-12} and 10^{-9} , covering the common values observed in nearby galaxies and the Milky Way. Although n has been updated with newer observations (Leroy et al. 2008; Bigiel et al. 2008), we opt to use the original value $n = 1.4$ because our model does not isolate molecular gas from cold ISM. The elements locked inside stars are stored separately from the ISM. The stars are stored in stellar bins sorted by initial mass.

Stellar mass bins are formed according to the Kroupa initial mass function from 0.08 to $50 M_{\odot}$ ($\alpha = 2.3$ if $m > 0.5 M_{\odot}$ and $\alpha = 1.3$ if $m \leq 0.5 M_{\odot}$) (Kroupa 2001). We do not consider stars with initial masses outside this range because they are not represented in the nucleosynthesis tables that we use. This leads to an underestimated a in the K-S law in our work, mostly due to missing low-mass stars. The stellar lifetimes are retrieved from PARSEC-1.2S isochrones from a grid of progenitor mass and metallicities (Bressan et al. 2012). The remaining mass bins are checked at each step to determine whether the stars in them should evolve.

3.1.3. Nucleosynthesis of elements

Nucleosynthesis is the main machinery that produces new elements. We adopt the yield tables Nomoto et al. (2013) which cover asymptotic giant branch (AGB) stars and core-collapse supernovae (CCSNe) and the WDD2 table from Iwamoto et al. (1999) for Type Ia supernovae

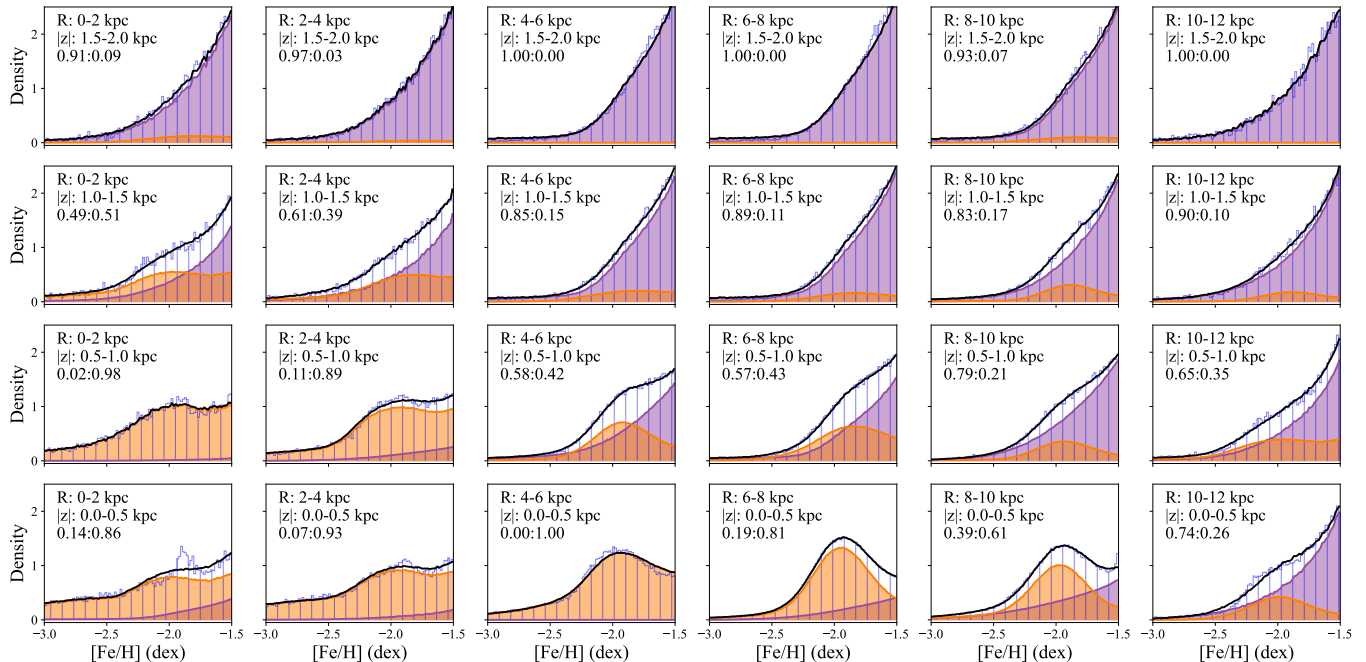


Figure 4. Reconstructing the observed metal-poor MDF using GCE models. The metal-poor MDF is presented as a function of R and $|z|$, with bin sizes of $\Delta R = 2$ kpc and $\Delta|z| = 0.5$ kpc. Observed MDFs (blue step histograms) are derived from the Gaia XP metallicity catalog by Zhang et al. (2023) and are modeled using two representative MDFs from our GCE models (purple and orange histograms) shown in Fig. 3. The relative proportions of these two MDFs are indicated below the R and $|z|$ range in each panel. The combined MDF, resulting from the weighted sum of the two representative MDFs, is depicted as a solid black line. The spatial variation in the observed metal-poor MDF across R and $|z|$ in the Gaia XP catalog is successfully explained by the combination of two distinct star formation scenarios.

(SNe Ia). We use the elemental versions, which list the mass of each element to be released. The table values for AGB and CCSNe are interpolated across a grid of metallicities and progenitor mass. The tables from these two nucleosynthesis channels list the stellar remnant mass for evolved stars within our mass range. The remnants of stars with $3 - 8 M_{\odot}$ are collected and stored in a white dwarf reservoir, a fraction f_{SNIa} of which produces the Chandrasekhar mass SNe Ia over an exponential timescale governed by $t_{\text{SNIa}} = 1.5$ Gyr. It is common to adopt a power law for the delay-time distribution (DTD) of SNe Ia from Maoz et al. (2012). However, the power law requires the maximum delay time to be set, which is not certain from observations. Our exponential law is sufficient to approximate the features of DTD from observations, including an early peak (< 0.4 Gyr), a sustained intermediate delay ($0.4 - 2.4$ Gyr) and a long-term delay (> 2.4 Gyr). $f_{\text{direct}} = 1\%$ of the newly produced yields is returned directly to cold ISM as a source of pollution, while the rest goes to warm ISM or escapes the galaxy through outflow.

3.1.4. Inflow and outflow

Today the amount of gas in the circumgalactic medium (CGM) is sufficient to sustain several M_{\odot} per

year of star formation for at least another Gyr (Richter et al. 2017), signifying that the Milky Way currently engages in material exchange with its surrounding environment with a predominant gas inflow into our Galaxy (Fox et al. 2019; Clark et al. 2022). The gas inflow would be more pronounced during the formative phase of the Milky Way when it was rapidly accreting mass and had elevated SFRs. We allow our model to accumulate warm gas from the CGM exponentially with a timescale t_{inflow} ranging from 100 Myr to 100 Gyr and a mass constant m_{inflow} ranging from 10^8 to $10^{12} M_{\odot}$, i.e. $\dot{m}_{\text{inflow}} = (m_{\text{inflow}}/t_{\text{inflow}}) \cdot e^{t/t_{\text{inflow}}}$. We assign the newly accreted gas to warm ISM because the temperature of the inflow gas is typically above 10^4 K (Joung et al. 2012; Zhang et al. 2021). On the other side, star formation and nucleosynthesis events trigger gas outflow with a mass loading factor $\eta_{\text{outflow}} = 0.1$ as estimated by Li et al. (2017); Fox et al. (2019); Kim et al. (2020). 1% of the newly produced yields is instantly returned to the cold ISM. This leaves 89% of nucleosynthesis yields in warm ISM for later star formation. Unlike heating, the gas outflow is considered lost to the model during the entire time span of our model.

3.2. Recovering observed MDFs

We ran our one-zone GCE model 50,000 times with individually independently randomly generated parameters within the ranges specified above. 14,302 models successfully reached $[\text{Fe}/\text{H}] = -1.5$ after 1.5 Gyr of runtime and formed less than $5 \times 10^9 M_\odot$ of stars. We generated a $[\text{Fe}/\text{H}]$ sample from each of these models with $\Delta[\text{Fe}/\text{H}] = 0.1$ dex which produces larger spreads at low metallicities at a given time step. After generating the metallicity samples, we identified the best matching MDFs to the observed ones at high- $|z|$ and low- $|z|$ regions in Fig. 1. We normalized the MDFs and calculated the difference over a targeted metallicity range. For the observed ascending exponential MDFs at high- $|z|$, we had an abundance of matched MDFs from our GCE models and thus calculated the difference over $-3.0 < [\text{Fe}/\text{H}] < -1.5$. However, it was much more difficult to identify bell-shaped MDFs at low- $|z|$ so we targeted $-2.0 < [\text{Fe}/\text{H}] < -1.5$ where the stellar density was declining and did not require the peak at $[\text{Fe}/\text{H}] \approx -2.0$. These two categories of MDFs are organically produced through our GCE models.

The design of our original model is insufficient to match the observed bell-shaped MDF. Due to the exponential inflow function and fixed ϵ_{KS} we adopted, we can only have a single star formation burst in the beginning. As a result, the peak metallicities in our bell-shaped MDFs are always too low and the spread in the MDFs are too wide. Thus, we designed a separate GCE model with a flexible SFR adjustable at each time step to generate a third category of MDFs matching the ones at low- $|z|$. We selected 2,000 models that best match the observed low- $|z|$ bell-shaped MDFs up to $[\text{Fe}/\text{H}] = -2.5$ and used their initial conditions as setups for the second GCE run. At each time step, the model calculates the SFR by comparing the relative number of newly formed stars against the observed stellar density at the corresponding $[\text{Fe}/\text{H}]$. The model is allowed additional inflowing gas when the existing cold gas reservoir cannot sustain the desired SFR according to the K-S law in Section 3.1.2. We manage to obtain MDFs with peaks at $[\text{Fe}/\text{H}] \approx -2.0$ from our GCE models as a result. Even though the modified models could exceed our initial stellar mass limit of $5 \times 10^9 M_\odot$, we choose to keep only those under the limit.

Figure 3 summarizes the three categories of MDFs generated with our models. The top panels illustrate the star formation histories (SFHs) that lead to the MDFs from our GCE models and the bottom panels showcase examples of MDFs over the possible range of stellar mass. The two columns on the left are for organically produced bell-shaped and ascending exponential MDFs and the last column is for bell-shaped MDFs

with its peak at $[\text{Fe}/\text{H}] \approx -2.0$ due to the implementation of a flexible SFR. We matched the SFHs based on the shapes of the MDFs after normalization due to the large discrepancies in the number of stars among different panels. In the top panels, the black solid lines represent the median SFHs derived for the three MDF shapes. The dark- and light-shaded regions enclose one sigma and two sigmas of possible SFRs. The slashed regions indicate when the stellar bins reach $[\text{Fe}/\text{H}] = -2.0$ in the GCE models. In the top left panel, the bell-shaped MDFs organically produced by our GCE models typically have a peak metallicity of around -3.0 and correspond to a maximum median SFR of about $60 M_\odot$ per year (capable of reaching above $100 M_\odot$ per year). The SFR declines exponentially rapidly and reaches around $10 M_\odot$ per year after one Gyr since the first stars formed in the model. A similar star formation burst can be seen in the top right panel, but the median SFR is lowered to around $30 M_\odot$ per year. The timing of the metallicity peak is delayed by around 300 Myrs but still within the first Gyr.

As the MDFs in the leftmost columns of Fig. 3 are too metal-poor and have a greater spread than observed, we opt to use the MDFs represented in the middle and right columns. These two categories of MDFs already resemble those observed at high- $|z|$ and low- $|z|$ panels respectively. We use them as candidates for approximating the relative contributions of the two star formation scenarios at different spatial locations. Figure 4 shows the same observed MDF as a function of R and $|z|$ as in Fig. 1 except with finer ($R, |z|$) bins fitted with MDFs derived from our GCE models. The observed histogram is shown in a blue step histogram in the background of each panel. The two shaded histograms correspond to the two GCE-modeled MDFs used in fitting the observed MDF in each panel. The black line indicates the final fitted MDF. Overall, two GCE-modeled MDFs can well approximate the observed MDFs within our range of R and $|z|$. The relative contribution between the two MDFs used in each panel is listed in the top left corner.

The bell-shaped MDF is the most prominent in regions closest to the Galactic center and in the disk plane with low- $|z|$. The ascending exponential MDF takes over as R and $|z|$ increases. To further illustrate the visibility of the starburst population as quantified by the relative contribution of the bell-shaped MDF, we randomly chose 10,000 locations within our range of R and z and repeated the same fitting process with GCE-modeled MDFs for the local observed MDF. We required the region to have at least 5,000 stars in order to be fitted. The result is shown in Figure 5 in which the prominence of the metal-poor peak varies with R and z . Here

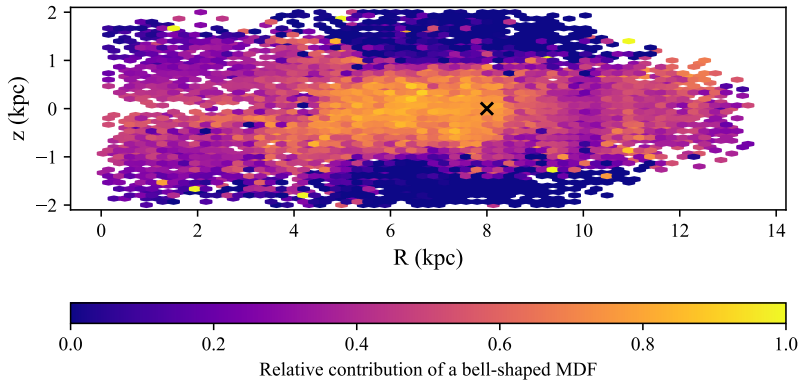


Figure 5. Visibility map of the metallicity density peak at $[\text{Fe}/\text{H}] = -2.0$ across the Galactic disk. We randomly chose 10,000 locations in the Galactocentric coordinates (R, z) and fitted the MDF in each location within a radius of 1 kpc in (x, y, z) with templates from our GCE models. The relative weight of the starburst GCE model represented in the rightmost panel in Fig. 3 is obtained for each location and shown in color. The density peak we study in the work is visible in the bulge region to higher z but only visible under $|z| = 1$ kpc beyond 5 kpc.

we can see that the starburst metallicity peak is visible at high- $|z|$ when $R < 5$ kpc but is restricted to low- $|z|$ otherwise.

To sum up, we adopted a GCE model with flexible SFH in order to explicitly match the bell-shaped MDF seen in low- $|z|$ regions. Fig. 3 shows that a star formation burst in the first Gyr with a median peak SFR of 40 M_{\odot} per year is required to reproduce the observed bell-shaped MDF. The ascending exponential MDF can arise from steady star formation afterward. The MDFs associated with these two star formation scenarios are sufficiently displaced within our targeted metallicity range ($-3.0 < [\text{Fe}/\text{H}] < -1.5$), which allows us to disentangle them. It would have also been impossible to detect the starburst if the proto-Galaxy had a heightened SFR throughout its formation period. Fig. 4 and 5 show the visibility of the $[\text{Fe}/\text{H}] = -2.0$ peak as a function of R and z in detail. They suggest that this starburst population resides in the disk plane up to $|z| = 1.0$ kpc, but it can extend up to $|z| = 2.0$ kpc when $R < 5$ kpc.

4. STARBURSTS IN AURIGA SIMULATIONS

This study leverages a suite of advanced simulations of galaxies with virial masses of $1 - 2 \times 10^{12} M_{\odot}$ similar to our Galaxy, drawn from the AURIGA project (Grand et al. 2024). Auriga provides a unique window into galaxy formation, employing thirty high-resolution magneto-hydrodynamic simulations that follow the evolution of individual galaxies within a realistic cosmological environment. The general agreement between Auriga galaxies and our own is reflected in a variety of key characteristics, including the relationship between halo mass and metallicity (Monachesi et al. 2019), the oscillations within their galactic discs (Gómez et al. 2017a), their rotation curves and star formation rates (Grand

et al. 2017), the distinct structure of their thin and thick discs (Grand et al. 2018; Pinna et al. 2024), and the detailed chemical and dynamical properties of their central regions (Fragkoudi et al. 2020). Unlike simulations tailored to reproduce the specific characteristics of our own galaxy, Auriga explores a diverse range of possible formation histories, offering a broader perspective on the processes that shape galaxies like ours.

Auriga uses cosmological parameters from Planck Collaboration et al. (2014) and has a dark matter and baryonic element resolution of $\sim 3 \times 10^5 M_{\odot}$ and $\sim 5 \times 10^4 M_{\odot}$, respectively, at the standard “level-4” resolution. Each simulation provides 128 snapshots, capturing the evolution of the galaxies from the early universe (redshift $z = 127$) to the present day ($z = 0$). The simulations incorporate a self-consistent physical model for the behavior of baryonic matter, including the radiative cooling of gas, the formation of stars, the feedback effects of stellar evolution and supernova explosions, the growth and influence of supermassive black holes, and the dynamics of magnetic fields. These intricate sub-grid physics models, meticulously described in Grand et al. (2017), have been rigorously tested and validated in previous cosmological simulations (Vogelsberger et al. 2013; Genel et al. 2014; Marinacci et al. 2014), demonstrating their ability to reproduce a wide array of observed galaxy properties.

We pick four Milky Way-analogs, Auriga-2, 12, 23, 24, for comparison with our observational data and GCE models due to their prominent early star formation bursts. For each analog galaxy, we isolate the earliest starburst event that includes a sufficient number of star particles. Figure 6 demonstrates the present-day MDFs and SFHs for three populations on halo-like orbits in each simulated galaxy: accreted stars (gray), in situ

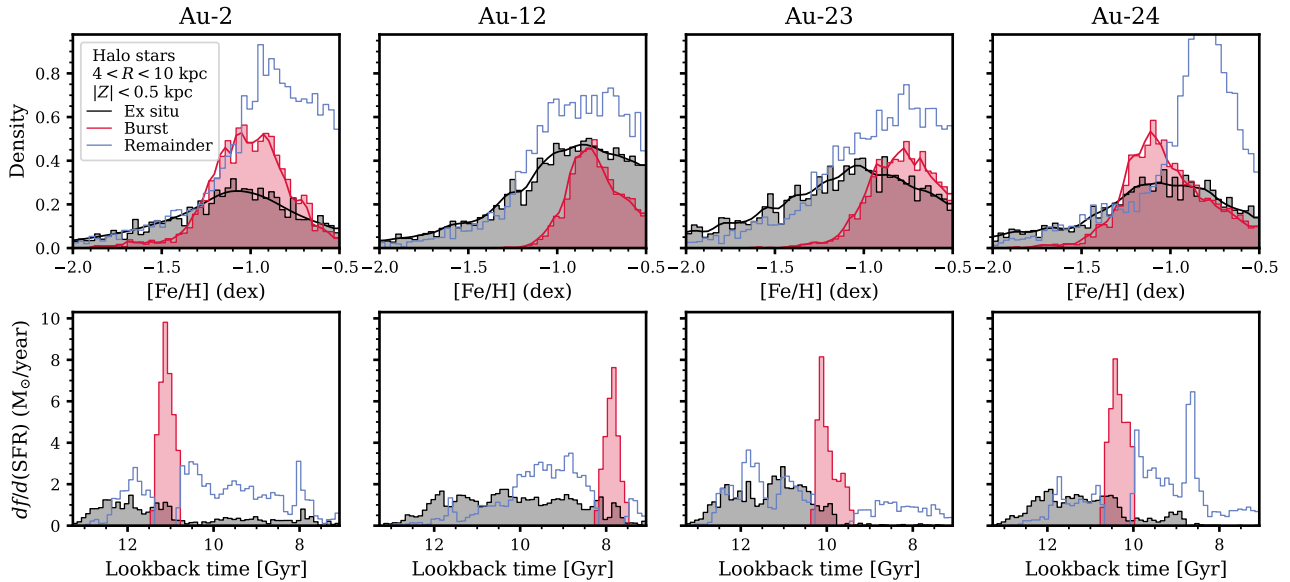


Figure 6. MDFs and SFHs of starburst populations versus other old non-disk populations in four Milky Way analogs, Auriga-2, 12, 23 and 24. The panels in the top row indicate the present-day stellar distribution of $[\text{Fe}/\text{H}]$ of the earliest starbursts (red), the accreted or ex situ stars (gray), and the rest of in situ stars (blue) in the region where $|z| < 0.5$ and $4 < R < 10$ kpc in the first several Gyrs in the galaxies. The SFHs for the same populations are represented in the same style in the bottom panels. The starbursts in these four galaxies only last a few hundred Myrs and produce bell-shaped MDFs with limited spreads compared to the rest of the old stars.

starburst (red), and the rest of the old stars on halo-like orbits (blue) within $4 < R < 10$ kpc and $|z| < 0.5$ kpc. One feature of the nucleosynthesis in Auriga is that it generates a considerable spread in metallicity and thus metallicity is not closely associated with age even in the metal-poor regime. To solve this issue, only star particles older than 7.5 Gyr and located on halo-like orbits are chosen for Fig. 6. To identify stars on halo-like orbits, we used the distribution of the circularity parameter shown below to assign a probability of belonging to the halo, p_{halo} .

$$\epsilon_{\text{circ}} = \frac{L_z}{L_z^{\text{max}}(E)} \quad (1)$$

where L_z is the z -component of the angular momentum, and $L_z^{\text{max}}(E)$ is the maximum angular momentum that is allowed for the given specific orbital energy. This method is commonly used in simulations (see Abadi et al. (2003); Grand et al. (2017); Gómez et al. (2017b)). We place an additional constraint of $-2.0 < [\text{Fe}/\text{H}] < -0.5$ on the sample in the bottom panel so that the top and bottom panels display the same stars. The star formation bursts last only a few hundred Myr and reach their peak SFR for less than 100 Myr. These bursts leave behind bell-shaped MDFs with a narrower spread compared to the other two populations, closely resembling those observed in the Gaia XP catalog. However, the metallicity values of the simulated starbursts are higher than those observed. Al-

though starbursts occur prior to 12 Gyr in lookback time, they typically consist of only a few hundred star particles, insufficient for a detailed study of their properties. Consequently, the simulated starbursts tend to be younger, and their metallicity distributions overlap with stars that formed before or after the burst, in contrast to the observed metallicity peak that dominates the metallicity range.

Figure 7 displays the present-day spatial distribution of galactocentric coordinates in both the (R, z) and (x, y) planes. For each Auriga galaxy, the left panels show the spatial density distribution of the entire galaxy, which includes stars on disk orbits, while the right panels depict the starburst population, along with their respective stellar masses. When showing the entire galaxy, the samples in this and subsequent figures include stars on disk orbits. The starburst populations are confined close to the disk plane and exhibit a strong central concentration toward the galactic center, with density cutoffs occurring around $R = 5$ kpc. In the (x, y) plane, the density distributions of the starburst populations align with the orientation of the entire galaxy but appear more extended in the transverse direction. During starburst events, inflowing gas is typically funneled toward the galactic center, where the majority of star formation occurs. Over time, these stars migrate outward, and their orbits become dynamically heated due to interactions within the disk.

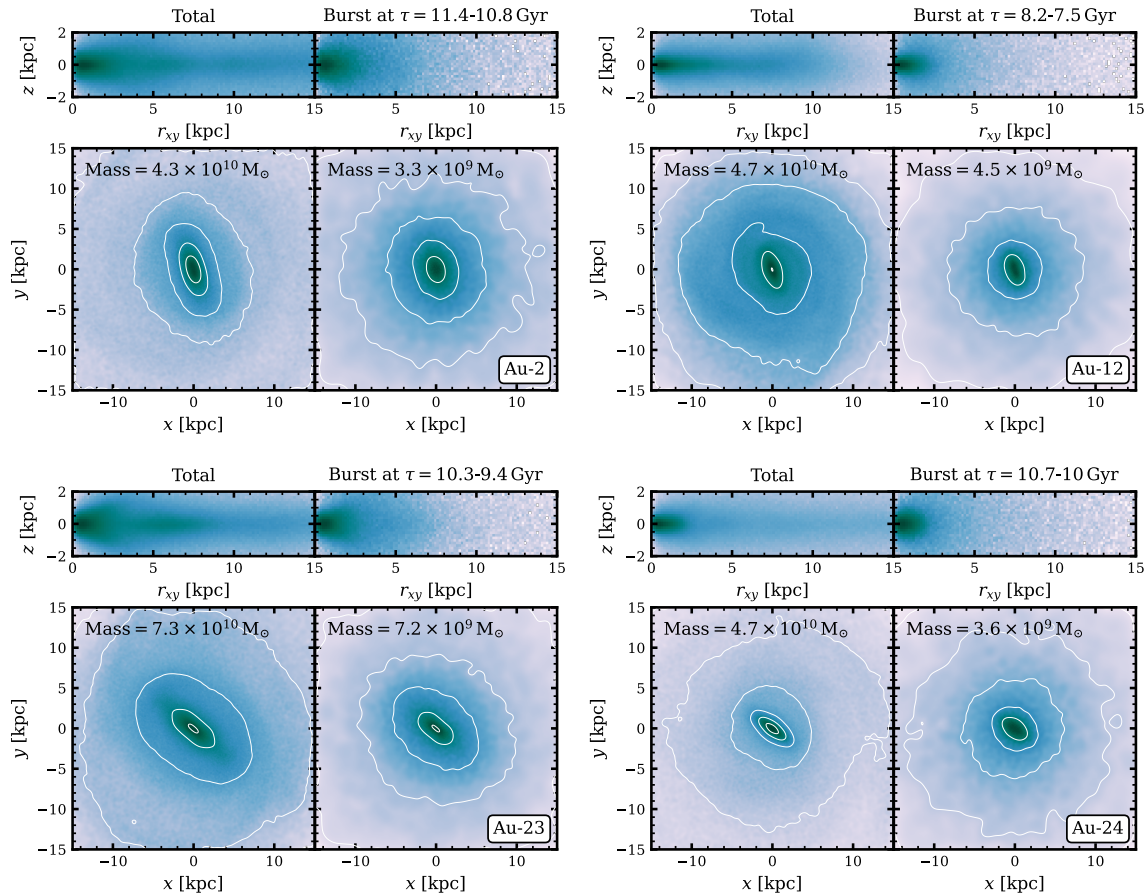


Figure 7. Present-day ($z=0$) spatial density distribution of star particles in the entire galaxy vs. an early starburst population in our Auriga galaxies. The edge-on view in (R, z) and the top-down view in (x, y) are shown for both populations in each galaxy. The density scale is normalized for each population. The stellar mass for each population is listed in the top left corner of each panel. The timing of the burst is shown above the (R, z) panel for each starburst population.

Figure 8 shows the present-day galactocentric radial and azimuthal velocities (v_r, v_ϕ) for three distinct populations in our Auriga galaxies: the entire galaxy, the in situ starburst population, and the accreted population directly responsible for the associated star formation bursts. To ensure consistency with the spatial distributions shown in Fig. 7, a vertical cut of $|z| < 2$ kpc is applied to all samples. The solid horizontal lines indicate the median v_ϕ for each population to provide a reference for their rotational behavior. All Auriga galaxies exhibit rotation velocities similar to that of the Sun in the Milky Way, approximately 200 km/s, reflecting their disk-like kinematics. The starburst populations show a range of v_ϕ values from 0 to 100 km/s, indicating slower rotation compared to the overall galaxy. The accreted populations, while sharing similar median v_ϕ values, display a narrower spread in rotational velocities. Notably, the accreted population of Auriga-24 exhibits less spread in v_ϕ compared to the other galaxies, resembling the Gaia sausage. These velocity dis-

tributions align with the observed residual v_ϕ in Fig. 2, which reveals a possible lagging rotation for the observed starburst population. This lagging rotation is consistent with the idea that these stars formed during an ancient burst and have since experienced dynamical heating or migration within the disk.

5. DISCUSSION

Earlier studies of the metal-poor MDFs were restricted by the size or spatial coverage of their samples. Our work presents the most comprehensive evidence of the varying metallicity distributions and the resulting physical conditions in the proto-Galaxy, thanks to the metallicity estimates made available from the Gaia XP spectra. We found that the metal-poor MDFs in the disk plane take a bell shape with peak metallicities around $[\text{Fe} / \text{H}] = -2.0$, which increases slightly with R . As we examine regions farther from the disk plane, the MDFs shift to an ascending shape typically resulting from a stable or intensifying SFH.

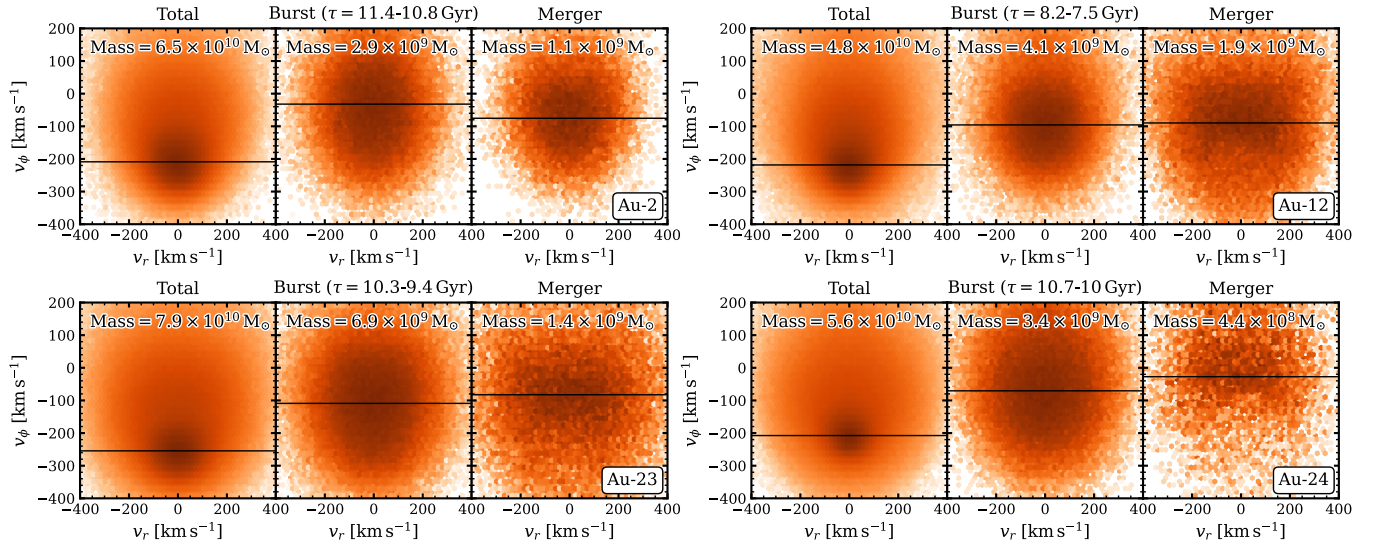


Figure 8. Present-day ($z=0$) distribution of the galactocentric radial velocity (v_r) and azimuthal velocity (v_ϕ) in the cylindrical coordinates of the entire galaxy, an early starburst population, and the accreted population causing the burst in our four Auriga galaxies. The total mass of star particles in each panel is listed in the top left corner. The solid horizontal lines mark the median v_ϕ for each population.

A bell-shaped metal-poor MDF with mean $[\text{Fe}/\text{H}] \approx -1.5$ had been first observed and replicated with a closed-box GCE model by Hartwick (1976), though several peaks with different metallicities were present in their sample (see their Figure 2). Chiba & Beers (2000) found a group of stars on high-eccentricity orbits centered at $[\text{Fe}/\text{H}] = -1.7$. Similar bell-shaped MDFs with peaks between $-2.5 < [\text{Fe}/\text{H}] < -1.5$ have been identified and dynamically assigned to the halo away from the disk plane in recent studies (An et al. 2013; Liu et al. 2018; Youakim et al. 2020). Bensby et al. (2013) and Ness & Freeman (2016) studied the detailed chemical distribution in the bulge, which also revealed an excess of stars with $-2.0 < [\text{Fe}/\text{H}] < -1.5$ after fitting the bulge MDF with Gaussian components. Chiba & Beers (2000) and de Jong et al. (2010) found that the median metallicity shifts with high uncertainty within $-3.0 < [\text{Fe}/\text{H}] < -1.5$ according to locations in the sky. Chiti et al. (2021) revealed a subtle correlation between the slope of the metal-poor tail of the MDF below $[\text{Fe}/\text{H}] = -2.0$ and height from the disk plane. These early studies suggest that clues to the earliest epoch of the Milky Way could be hiding among metal-poor stars, but they either lacked a large sample or did not show a clear spatial variation of the metal-poor MDF in the Galaxy. Hayden et al. (2015) prominently showed that the MDFs in the disk with $[\text{Fe}/\text{H}] > -1$ vary with R and $|z|$ up to $|z| = 1$ kpc. We confirm that the same holds true in the metal-poor regime.

The physical conditions inferred from our GCE models are consistent with recent findings on the proto-Galaxy.

Rix et al. (2022) used a subset of the sample in this work to reveal a concentration of metal-poor stars near the Galactic center up to $10^8 M_\odot$ that could be remnants of the earliest epoch of our Galaxy. They calculated the gas inflow rate from the slope of the metal-poor tail of the MDF with an analytic GCE model and found that the inflow rate must be close to zero. Chen et al. (2024) used a GCE model similar to the one outlined in this work to replicate the unexpected increase in $[\text{Mg}/\text{Fe}]$ found by Conroy et al. (2022) and Belokurov & Kravtsov (2022) and concluded that a large amount of high- $[\alpha/\text{Fe}]$ inflow gas joined the Galaxy after the initial phase with limited inflow. Our work showed that the metal-poor MDF is composed of two distinct MDFs, a centrally concentrated bell-shaped MDF and a spatially extended ascending exponential MDF. The scenario with limited inflow applies only to the second MDF which indicates a gradual build-up of stellar mass towards a higher metallicity. The first MDF, however, suggests a different scenario under which around $10^9 M_\odot$ of stars formed within a few hundred million years. It is likely that the proto-Galaxy was quiescent by default but was disturbed by a few key short-lived events that produced the majority of its stellar mass. Ardern-Arentsen et al. (2024) curated a large sample of metal-poor stars with $[\text{Fe}/\text{H}]$ down to -3.0 near the Galactic center ($|l| < 12^\circ$) and managed to identify two components. However, their sample lacked stars with $|z| < 0.35$ kpc which constitute the bell-shaped MDF.

The origin of the central metal-poor population remains a subject of debate and an open question in galac-

tic archaeology. Belokurov & Kravtsov (2022) proposed that this population represents the in situ stars of the proto-Galaxy, designating it as *Aurora* due to its negligible net rotation. Belokurov & Kravtsov (2023) and Belokurov & Kravtsov (2024) further characterized Aurora’s chemodynamical properties and established quantitative selection criteria for its identification. However, their analysis relied on APOGEE data, which lacks stars with $[\text{Fe}/\text{H}] < -1.5$, raising the possibility that the observed Aurora population may only represent a subset of the in situ stars from the proto-Galaxy. Alternatively, this central population could have originated from a major accretion event during an earlier, less massive phase of the Galaxy. For instance, Kruijssen et al. (2020) identified a massive accreted structure, *Kraken* ($M \approx 10^9 M_\odot$), through simulations of globular clusters analogous to those in the Milky Way. Similarly, Horta et al. (2021) discovered another accreted structure in the bulge, *Hercules*, with a mass of $M \approx 5 \times 10^8 M_\odot$ and a metallicity peak around $[\text{Fe}/\text{H}] = -1.3$. Despite these discoveries, disentangling in situ from ex situ populations remains challenging both kinematically and chemically early in our Galaxy (Orkney et al. 2022).

Simulated analogs of the Milky Way suggest that the origin of old stars may vary depending on the epoch. El-Badry et al. (2018) demonstrated that the oldest and most metal-poor stars in FIRE Milky Way-analogs are predominantly accreted through the hierarchical merging of low-mass halos, with subsequent star formation primarily occurring in the central regions. Similarly, Horta et al. (2024) found in FIRE-2 simulations that Milky Way-like galaxies typically form from one or two major progenitors accompanied by several smaller ones, indicating a mixed origin for their stellar populations. Our work builds on these findings, providing new insights into the central metal-poor population. We reveal that an ancient burst of central star formation, likely occurring after the hierarchical assembly of the proto-Galaxy, could explain the observed spatial distribution of this population. Furthermore, our simulations show that accreted populations could not produce the observed MDF, suggesting that the majority of these stars likely formed in situ.

The limited vertical spatial distribution of the starburst population could be a natural consequence of disk evolution. Unlike previous metal-poor MDF studies targeting high- $|z|$ regions, the density peak at $[\text{Fe}/\text{H}] \approx -2.0$ is restricted to $|z| < 2$ kpc in our Fig. 5. The early starburst populations in Auriga mirror similar distributions in the disks in Fig. 7 in both (R, z) and (x, y) . Despite the star formation burst occurring near the center of the galaxies, many stars are found at large radii

up to $R = 5$ kpc in the $z=0$ snapshot through radial migration. The maximum $|z|$ -height of the Auriga starburst populations is higher than the observations imply but largely consistent with the disks. The lack of disk thickening or the inability of disk mechanisms to heat up stars vertically has been shown in simulations by Minchev et al. (2012); Halle et al. (2015); Vera-Ciro et al. (2016); Aumer et al. (2017); Agertz et al. (2021). Focusing on APOGEE/Gaia data, Frankel et al. (2020) quantified the magnitudes of radial migration (change in the angular momentum of orbits) and vertical heating, finding that the strength of vertical heating is only about 10% that of radial migration in the last six Gyr. Recently, Hamilton et al. (2024) connected the physical mechanisms of the two through numerical simulations with one or multiple transient spiral arms but found it difficult to replicate the little vertical heating given the amount of radial migration in the Milky Way. Thus, the limited vertical heating implied by the visibility map of our observed starburst population matches the expected pattern for an ancient starburst population that was once centrally concentrated.

We extracted a signature of a slow-spinning structure with an azimuthal velocity of less than 100 km/s. This velocity is between the azimuthal velocity of the solar neighborhood at around 240 km/s and the non-rotation of the Gaia sausage. Similar slow-spinning structures have been identified before in the metal-poor regime among halo stars. For example, Tian et al. (2019) found the local halo to be rotating at 27 km/s with a dispersion of 72 km/s. Mardini et al. (2022) identified the *Atari* disk with $v_\phi \approx 150$ km/s over $-3.50 < [\text{Fe}/\text{H}] < -0.8$, which is more centrally concentrated with $h_R = 2.48$ kpc but more vertically extended with $h_z = 1.68$ kpc, compared to what we showed in Fig. 5. Cordoni et al. (2021) found dozens of metal-poor stars ($[\text{Fe}/\text{H}] < -2.0$) on prograde orbits with low eccentricities, which are not consistent with the GSE. An & Beers (2021) found the median v_ϕ of stars with $-3.0 < [\text{Fe}/\text{H}] < -2.2$ to be around 100 km/s but attributed this to a combination of the GSE and metal-weak thick disk (MWTD). More recently, Viswanathan et al. (2024) found that the high- α stars in our Galaxy gradually spun up over $-1.7 < [\text{Fe}/\text{H}] < -1.0$, leaving a substantial number of slow-spinning stars at low metallicity, as compared to the sharp spin-up initially shown by Belokurov & Kravtsov (2022). They suggested that the initial v_ϕ of the in situ proto-Milky Way could be non-zero but under 100 km/s. All of these stellar populations are restricted to the Galactic plane up to $|z_{\text{max}}| < 3$ kpc. Although our sample with radial velocity is small and most likely biased by selection effects, the residual v_ϕ

signature we identified in this work is consistent with the scenario of a slow-spinning in situ prototype population before the formation of the disk. This is supported by the starburst populations in Auriga galaxies which are also slow-spinning and have v_ϕ less than 100 km/s. However, the Auriga simulations also indicate that the ex situ populations could have similar v_ϕ and thus it would be difficult to disentangle the two populations to ascertain the v_ϕ value of the proto-Galaxy today.

Simulations have predicted that star formation bursts causing order of magnitude change in SFR should be common in low-mass galaxies at high redshift ($z > 7$) (Hopkins et al. 2014; Domínguez et al. 2015; Muratov et al. 2015; Sparre et al. 2017; Pallottini & Ferrara 2023). Star formation is temporarily suppressed when feedback from clusters of supernovae drives gas outflow and resumes when the gas cools (Hu et al. 2023). Star formation transitions from bursty to smooth as the potential well or inner virial mass and rotation support of galaxies builds up until cold gas filaments cannot participate in inflow and outflow (Stern et al. 2021; Gurvich et al. 2023; Byrne et al. 2023; Hopkins et al. 2023). Recent observations from the James Webb Space Telescope (JWST) have confirmed that starbursts are common among low-mass galaxies at $z \sim 6 - 12$ (Looser et al. 2023, 2024; Dressler et al. 2024; Endsley et al. 2024). Interestingly, starbursts can cause galaxies to appear more luminous, which could potentially explain the abundance of super-massive galaxies at high redshift (Sun et al. 2023). Ting & Ji (2024) employed an analytic GCE model to quantify starbursts in the Sculptor dSph dwarf galaxy, which typically last around 100 Myr and are separated by quiescent periods of approximately 300 Myr. Like many galaxies, our Galaxy would be much less massive at high redshift and should have gone through the phase of bursty star formation.

6. CONCLUSION

Our work takes advantage of the unprecedented volume of VMP and metal-poor stars from the Gaia XP spectra derived with data-driven methods. Although there are many Gaia XP metallicity catalogs, it remains difficult to identify one trained on a sufficiently large and consistent metal-poor sample. We selected stars with reliable metallicity measurements between $[\text{Fe}/\text{H}] = -3.0$ and -1.5 from Zhang et al. (2023) and identified two distinct MDFs in the high- and low- $|z|$ regions, a bell-shaped one and an ascending exponential one. Theoretically, an exponential MDF naturally forms in the low-metallicity regime as metallicity rapidly increases, as long as star formation remains stable. It is surprising to find a bell-shaped MDF as it would indicate a rapid

quenching in star formation, as commonly expected in low-mass galaxies. The two MDFs present two irreconcilable formation scenarios for the proto-Galaxy, which could be explained by two distinct events.

Our discovery reveals a new key metallicity milestone in the evolutionary history of our Galaxy at $[\text{Fe}/\text{H}] = -2.0$. A star formation burst near the center of our Galaxy was possibly triggered by an accretion event which brought in a large amount of gas, leading to a substantial amount of stars with $[\text{Fe}/\text{H}] \approx -2.0$. This starburst population precedes the GSE and serves as a likely candidate for the in situ proto-Galaxy. Here is a summary of our results from the Gaia XP catalog and our GCE models:

1. This population is the most visible close in the Galactic disk plane with $|z| < 1$ kpc but could extend up to $|z| = 2$ kpc in the bulge region, which alludes to its spatial distribution. The visibility in the (R, z) plane resembles the spatial stellar distribution of the disk.
2. v_ϕ in the residual velocity distribution changes sharply from -240 km/s to -100 km/s at $[\text{Fe}/\text{H}] = -2.4$ in the disk plane with $|z| < 0.5$ kpc, which could be a kinematic signature of the population. This signature is replaced by the Gaia Sausage at $v_\phi \approx 0$ km/s at higher metallicity and higher $|z|$.
3. The metallicity peak is caused by a brief star formation burst event within the first Gyr of our Galaxy ($z > 8$). The MDF as a function of R and $|z|$ can be explained by a superposition of two MDFs corresponding to two SFHs. The starburst population dominates the disk plane and the Galactic center, while the population in which stellar mass gradually builds up takes over elsewhere.

We examined the characteristics of the oldest starburst populations with sufficient star particles in four Auriga simulated Milky Way-analogs in order to determine the origin of the bell-shaped MDF and provide additional support to our observations. We found that the stellar mass of the accreted stellar population is normally a fraction of that formed in the subsequent in situ starburst in each galaxy. The starburst populations produce bell-shaped MDFs matching the ones observed in the Gaia XP data. Their current-day spatial distributions resemble the disk with a visible density cutoff at $R \sim 5 - 8$ kpc. This similarity could be explained by the disk mechanisms responsible for radial migration and vertical heating. They also have $v_\phi \sim -50 - 100$ km/s, consistent with the residual v_ϕ we extracted from

a small subset of our sample from the cross-match between Gaia XP and RVS. Therefore, we conclude that the stars in the bell-shaped MDF should be an in situ population of the proto-Galaxy.

The early evolutionary history of our Galaxy, preceding the formation of the disk, may have been characterized by significant dynamical and chemical complexity. During this epoch, star formation likely occurred in episodic bursts, separated by relatively quiescent intervals. These bursty SFHs are a natural outcome of feedback-regulated star formation in low-mass galaxies, as demonstrated by both cosmological simulations and recent observations with JWST. In this study, we identify evidence for one such starburst event in the proto-Galaxy, which likely contributed significantly to the early chemical enrichment of the Milky Way. However, the possibility remains that additional starbursts

occurred during this period, yet remain undetected due to limitations in the precision of current metallicity estimates.

Targeted follow-up observations of stars with metallicities in the range $-2.5 < [\text{Fe}/\text{H}] < -2.0$ in the Galactic plane could yield critical insights into the formation and characteristics of these populations. These stars are particularly valuable for reconstructing the detailed star formation history of the proto-Galaxy. Furthermore, as major mergers during the Galaxy's assembly are expected to substantially disrupt kinematic signatures (Laporte et al. 2019; Bland-Hawthorn et al. 2019), complementary approaches such as GCE models applied to large-scale stellar surveys will be essential. The integration of these models with observational data offers a powerful framework for disentangling the complex processes that shaped the early Milky Way in future studies of Galactic archaeology.

REFERENCES

- Abadi, M. G., Navarro, J. F., Steinmetz, M., & Eke, V. R. 2003, *ApJ*, 597, 21, doi: [10.1086/378316](https://doi.org/10.1086/378316)
- Agertz, O., Renaud, F., Feltzing, S., et al. 2021, *MNRAS*, 503, 5826, doi: [10.1093/mnras/stab322](https://doi.org/10.1093/mnras/stab322)
- An, D., & Beers, T. C. 2021, *ApJ*, 918, 74, doi: [10.3847/1538-4357/ac07a4](https://doi.org/10.3847/1538-4357/ac07a4)
- An, D., Beers, T. C., Johnson, J. A., et al. 2013, *ApJ*, 763, 65, doi: [10.1088/0004-637X/763/1/65](https://doi.org/10.1088/0004-637X/763/1/65)
- Andrae, R., Rix, H.-W., & Chandra, V. 2023a, *ApJS*, 267, 8, doi: [10.3847/1538-4365/acd53e](https://doi.org/10.3847/1538-4365/acd53e)
- Andrae, R., Fouesneau, M., Sordo, R., et al. 2023b, *A&A*, 674, A27, doi: [10.1051/0004-6361/202243462](https://doi.org/10.1051/0004-6361/202243462)
- Andrews, B. H., Weinberg, D. H., Schönrich, R., & Johnson, J. A. 2017, *ApJ*, 835, 224, doi: [10.3847/1538-4357/835/2/224](https://doi.org/10.3847/1538-4357/835/2/224)
- Ardern-Arentsen, A., Monari, G., Queiroz, A. B. A., et al. 2024, *MNRAS*, 530, 3391, doi: [10.1093/mnras/stae1049](https://doi.org/10.1093/mnras/stae1049)
- Astropy Collaboration, Price-Whelan, A. M., Lim, P. L., et al. 2022, *ApJ*, 935, 167, doi: [10.3847/1538-4357/ac7c74](https://doi.org/10.3847/1538-4357/ac7c74)
- Aumer, M., Binney, J., & Schönrich, R. 2017, *MNRAS*, 470, 3685, doi: [10.1093/mnras/stx1483](https://doi.org/10.1093/mnras/stx1483)
- Belokurov, V., Erkal, D., Evans, N. W., Koposov, S. E., & Deason, A. J. 2018, *MNRAS*, 478, 611, doi: [10.1093/mnras/sty982](https://doi.org/10.1093/mnras/sty982)
- Belokurov, V., & Kravtsov, A. 2022, *MNRAS*, 514, 689, doi: [10.1093/mnras/stac1267](https://doi.org/10.1093/mnras/stac1267)
- . 2023, *MNRAS*, 525, 4456, doi: [10.1093/mnras/stad2241](https://doi.org/10.1093/mnras/stad2241)
- . 2024, *MNRAS*, 528, 3198, doi: [10.1093/mnras/stad3920](https://doi.org/10.1093/mnras/stad3920)
- Bensby, T., Yee, J. C., Feltzing, S., et al. 2013, *A&A*, 549, A147, doi: [10.1051/0004-6361/201220678](https://doi.org/10.1051/0004-6361/201220678)
- Bigiel, F., Leroy, A., Walter, F., et al. 2008, *AJ*, 136, 2846, doi: [10.1088/0004-6256/136/6/2846](https://doi.org/10.1088/0004-6256/136/6/2846)
- Bland-Hawthorn, J., Sharma, S., Tepper-Garcia, T., et al. 2019, *MNRAS*, 486, 1167, doi: [10.1093/mnras/stz217](https://doi.org/10.1093/mnras/stz217)
- Brauer, K., Andales, H. D., Ji, A. P., et al. 2022, *ApJ*, 937, 14, doi: [10.3847/1538-4357/ac85b9](https://doi.org/10.3847/1538-4357/ac85b9)
- Bressan, A., Marigo, P., Girardi, L., et al. 2012, *MNRAS*, 427, 127, doi: [10.1111/j.1365-2966.2012.21948.x](https://doi.org/10.1111/j.1365-2966.2012.21948.x)
- Byrne, L., Faucher-Giguère, C.-A., Stern, J., et al. 2023, *MNRAS*, 520, 722, doi: [10.1093/mnras/stad171](https://doi.org/10.1093/mnras/stad171)
- Casagrande, L., Schönrich, R., Asplund, M., et al. 2011, *A&A*, 530, A138, doi: [10.1051/0004-6361/201016276](https://doi.org/10.1051/0004-6361/201016276)
- Chandra, V., Semenov, V. A., Rix, H.-W., et al. 2024, *ApJ*, 972, 112, doi: [10.3847/1538-4357/ad5b60](https://doi.org/10.3847/1538-4357/ad5b60)
- Chen, B., Hayden, M. R., Sharma, S., et al. 2023, *MNRAS*, 523, 3791, doi: [10.1093/mnras/stad1568](https://doi.org/10.1093/mnras/stad1568)
- Chen, B., Ting, Y.-S., & Hayden, M. 2024, *PASA*, 41, e063, doi: [10.1017/pasa.2024.56](https://doi.org/10.1017/pasa.2024.56)
- Chen, T., & Prantzos, N. 2025, arXiv e-prints, arXiv:2501.03342, doi: [10.48550/arXiv.2501.03342](https://doi.org/10.48550/arXiv.2501.03342)
- Chiba, M., & Beers, T. C. 2000, *AJ*, 119, 2843, doi: [10.1086/301409](https://doi.org/10.1086/301409)
- Chiti, A., Mardini, M. K., Frebel, A., & Daniel, T. 2021, *ApJL*, 911, L23, doi: [10.3847/2041-8213/abd629](https://doi.org/10.3847/2041-8213/abd629)
- Clark, S., Bordoloi, R., & Fox, A. J. 2022, *MNRAS*, 512, 811, doi: [10.1093/mnras/stac504](https://doi.org/10.1093/mnras/stac504)
- Conroy, C., Bonaca, A., Cargile, P., et al. 2019, *ApJ*, 883, 107, doi: [10.3847/1538-4357/ab38b8](https://doi.org/10.3847/1538-4357/ab38b8)

- Conroy, C., Weinberg, D. H., Naidu, R. P., et al. 2022, arXiv e-prints, arXiv:2204.02989, doi: [10.48550/arXiv.2204.02989](https://doi.org/10.48550/arXiv.2204.02989)
- Cooper, A. P., Cole, S., Frenk, C. S., et al. 2010, MNRAS, 406, 744, doi: [10.1111/j.1365-2966.2010.16740.x](https://doi.org/10.1111/j.1365-2966.2010.16740.x)
- Cordoni, G., Da Costa, G. S., Yong, D., et al. 2021, MNRAS, 503, 2539, doi: [10.1093/mnras/staa3417](https://doi.org/10.1093/mnras/staa3417)
- De Angeli, F., Weiler, M., Montegriffo, P., et al. 2023, A&A, 674, A2, doi: [10.1051/0004-6361/202243680](https://doi.org/10.1051/0004-6361/202243680)
- de Jong, J. T. A., Yanny, B., Rix, H.-W., et al. 2010, ApJ, 714, 663, doi: [10.1088/0004-637X/714/1/663](https://doi.org/10.1088/0004-637X/714/1/663)
- De Silva, G. M., Freeman, K. C., Bland-Hawthorn, J., et al. 2015, MNRAS, 449, 2604, doi: [10.1093/mnras/stv327](https://doi.org/10.1093/mnras/stv327)
- Domínguez, A., Siana, B., Brooks, A. M., et al. 2015, MNRAS, 451, 839, doi: [10.1093/mnras/stv1001](https://doi.org/10.1093/mnras/stv1001)
- Dressler, A., Rieke, M., Eisenstein, D., et al. 2024, ApJ, 964, 150, doi: [10.3847/1538-4357/ad1923](https://doi.org/10.3847/1538-4357/ad1923)
- El-Badry, K., Bland-Hawthorn, J., Wetzel, A., et al. 2018, MNRAS, 480, 652, doi: [10.1093/mnras/sty1864](https://doi.org/10.1093/mnras/sty1864)
- Endsley, R., Chisholm, J., Stark, D. P., Topping, M. W., & Whitley, L. 2024, arXiv e-prints, arXiv:2410.01905, doi: [10.48550/arXiv.2410.01905](https://doi.org/10.48550/arXiv.2410.01905)
- Fallows, C. P., & Sanders, J. L. 2024, MNRAS, 531, 2126, doi: [10.1093/mnras/stae1303](https://doi.org/10.1093/mnras/stae1303)
- Fox, A. J., Richter, P., Ashley, T., et al. 2019, ApJ, 884, 53, doi: [10.3847/1538-4357/ab40ad](https://doi.org/10.3847/1538-4357/ab40ad)
- Fragkoudi, F., Grand, R. J. J., Pakmor, R., et al. 2020, MNRAS, 494, 5936, doi: [10.1093/mnras/staa1104](https://doi.org/10.1093/mnras/staa1104)
- Frankel, N., Sanders, J., Ting, Y.-S., & Rix, H.-W. 2020, ApJ, 896, 15, doi: [10.3847/1538-4357/ab910c](https://doi.org/10.3847/1538-4357/ab910c)
- Freeman, K., & Bland-Hawthorn, J. 2002, ARA&A, 40, 487, doi: [10.1146/annurev.astro.40.060401.093840](https://doi.org/10.1146/annurev.astro.40.060401.093840)
- Gaia Collaboration, Vallenari, A., Brown, A. G. A., et al. 2023, A&A, 674, A1, doi: [10.1051/0004-6361/202243940](https://doi.org/10.1051/0004-6361/202243940)
- Genel, S., Vogelsberger, M., Springel, V., et al. 2014, MNRAS, 445, 175, doi: [10.1093/mnras/stu1654](https://doi.org/10.1093/mnras/stu1654)
- Gómez, F. A., White, S. D. M., Grand, R. J. J., et al. 2017a, MNRAS, 465, 3446, doi: [10.1093/mnras/stw2957](https://doi.org/10.1093/mnras/stw2957)
- Gómez, F. A., Grand, R. J. J., Monachesi, A., et al. 2017b, MNRAS, 472, 3722, doi: [10.1093/mnras/stx2149](https://doi.org/10.1093/mnras/stx2149)
- Grand, R. J. J., Fragkoudi, F., Gómez, F. A., et al. 2024, MNRAS, 532, 1814, doi: [10.1093/mnras/stae1598](https://doi.org/10.1093/mnras/stae1598)
- Grand, R. J. J., Gómez, F. A., Marinacci, F., et al. 2017, MNRAS, 467, 179, doi: [10.1093/mnras/stx071](https://doi.org/10.1093/mnras/stx071)
- Grand, R. J. J., Bustamante, S., Gómez, F. A., et al. 2018, MNRAS, 474, 3629, doi: [10.1093/mnras/stx3025](https://doi.org/10.1093/mnras/stx3025)
- Green, G. M., Schlafly, E., Zucker, C., Speagle, J. S., & Finkbeiner, D. 2019, ApJ, 887, 93, doi: [10.3847/1538-4357/ab5362](https://doi.org/10.3847/1538-4357/ab5362)
- Gurvich, A. B., Stern, J., Faucher-Giguère, C.-A., et al. 2023, MNRAS, 519, 2598, doi: [10.1093/mnras/stac3712](https://doi.org/10.1093/mnras/stac3712)
- Halle, A., Di Matteo, P., Haywood, M., & Combes, F. 2015, A&A, 578, A58, doi: [10.1051/0004-6361/201525612](https://doi.org/10.1051/0004-6361/201525612)
- Hamilton, C., Modak, S., & Tremaine, S. 2024, arXiv e-prints, arXiv:2411.08944, doi: [10.48550/arXiv.2411.08944](https://doi.org/10.48550/arXiv.2411.08944)
- Hartwick, F. D. A. 1976, ApJ, 209, 418, doi: [10.1086/154735](https://doi.org/10.1086/154735)
- Hattori, K. 2024, arXiv e-prints, arXiv:2404.01269, doi: [10.48550/arXiv.2404.01269](https://doi.org/10.48550/arXiv.2404.01269)
- Hayden, M. R., Bovy, J., Holtzman, J. A., et al. 2015, ApJ, 808, 132, doi: [10.1088/0004-637X/808/2/132](https://doi.org/10.1088/0004-637X/808/2/132)
- Helmi, A. 2020, ARA&A, 58, 205, doi: [10.1146/annurev-astro-032620-021917](https://doi.org/10.1146/annurev-astro-032620-021917)
- Helmi, A., Babusiaux, C., Koppelman, H. H., et al. 2018, Nature, 563, 85, doi: [10.1038/s41586-018-0625-x](https://doi.org/10.1038/s41586-018-0625-x)
- Hopkins, P. F., Kereš, D., Oñorbe, J., et al. 2014, MNRAS, 445, 581, doi: [10.1093/mnras/stu1738](https://doi.org/10.1093/mnras/stu1738)
- Hopkins, P. F., Gurvich, A. B., Shen, X., et al. 2023, MNRAS, 525, 2241, doi: [10.1093/mnras/stad1902](https://doi.org/10.1093/mnras/stad1902)
- Horta, D., Schiavon, R. P., Mackereth, J. T., et al. 2021, MNRAS, 500, 1385, doi: [10.1093/mnras/staa2987](https://doi.org/10.1093/mnras/staa2987)
- Horta, D., Cunningham, E. C., Sanderson, R., et al. 2024, MNRAS, 527, 9810, doi: [10.1093/mnras/stad3834](https://doi.org/10.1093/mnras/stad3834)
- Hu, C.-Y., Smith, M. C., Teyssier, R., et al. 2023, ApJ, 950, 132, doi: [10.3847/1538-4357/accf9e](https://doi.org/10.3847/1538-4357/accf9e)
- Imig, J., Price, C., Holtzman, J. A., et al. 2023, ApJ, 954, 124, doi: [10.3847/1538-4357/ace9b8](https://doi.org/10.3847/1538-4357/ace9b8)
- Iwamoto, K., Brachwitz, F., Nomoto, K., et al. 1999, ApJS, 125, 439, doi: [10.1086/313278](https://doi.org/10.1086/313278)
- Johnson, J. W., Weinberg, D. H., Vincenzo, F., et al. 2021, MNRAS, 508, 4484, doi: [10.1093/mnras/stab2718](https://doi.org/10.1093/mnras/stab2718)
- Joung, M. R., Putman, M. E., Bryan, G. L., Fernández, X., & Peek, J. E. G. 2012, ApJ, 759, 137, doi: [10.1088/0004-637X/759/2/137](https://doi.org/10.1088/0004-637X/759/2/137)
- Kane, S. G., Belokurov, V., Cranmer, M., et al. 2024, arXiv e-prints, arXiv:2409.00197, doi: [10.48550/arXiv.2409.00197](https://doi.org/10.48550/arXiv.2409.00197)
- Kennicutt, Robert C., J. 1998, ApJ, 498, 541, doi: [10.1086/305588](https://doi.org/10.1086/305588)
- Khalatyan, A., Anders, F., Chiappini, C., et al. 2024, arXiv e-prints, arXiv:2407.06963, doi: [10.48550/arXiv.2407.06963](https://doi.org/10.48550/arXiv.2407.06963)
- Kim, C.-G., Ostriker, E. C., Somerville, R. S., et al. 2020, ApJ, 900, 61, doi: [10.3847/1538-4357/aba962](https://doi.org/10.3847/1538-4357/aba962)
- Kobayashi, C., Umeda, H., Nomoto, K., Tominaga, N., & Ohkubo, T. 2006, ApJ, 653, 1145, doi: [10.1086/508914](https://doi.org/10.1086/508914)
- Kroupa, P. 2001, MNRAS, 322, 231, doi: [10.1046/j.1365-8711.2001.04022.x](https://doi.org/10.1046/j.1365-8711.2001.04022.x)

- Kruijssen, J. M. D., Pfeffer, J. L., Reina-Campos, M., Crain, R. A., & Bastian, N. 2019, *MNRAS*, 486, 3180, doi: [10.1093/mnras/sty1609](https://doi.org/10.1093/mnras/sty1609)
- Kruijssen, J. M. D., Pfeffer, J. L., Chevance, M., et al. 2020, *MNRAS*, 498, 2472, doi: [10.1093/mnras/staa2452](https://doi.org/10.1093/mnras/staa2452)
- Kubryk, M., Prantzos, N., & Athanassoula, E. 2015, *A&A*, 580, A126, doi: [10.1051/0004-6361/201424171](https://doi.org/10.1051/0004-6361/201424171)
- Laporte, C. F. P., Minchev, I., Johnston, K. V., & Gómez, F. A. 2019, *MNRAS*, 485, 3134, doi: [10.1093/mnras/stz538](https://doi.org/10.1093/mnras/stz538)
- Laroche, A., & Speagle, J. S. 2024, arXiv e-prints, arXiv:2404.07316, doi: [10.48550/arXiv.2404.07316](https://doi.org/10.48550/arXiv.2404.07316)
- Lee, Y. S., Beers, T. C., An, D., et al. 2011, *ApJ*, 738, 187, doi: [10.1088/0004-637X/738/2/187](https://doi.org/10.1088/0004-637X/738/2/187)
- Leroy, A. K., Walter, F., Brinks, E., et al. 2008, *AJ*, 136, 2782, doi: [10.1088/0004-6256/136/6/2782](https://doi.org/10.1088/0004-6256/136/6/2782)
- Li, H., Aoki, W., Matsuno, T., et al. 2022, *ApJ*, 931, 147, doi: [10.3847/1538-4357/ac6514](https://doi.org/10.3847/1538-4357/ac6514)
- Li, J., Wong, K. W. K., Hogg, D. W., Rix, H.-W., & Chandra, V. 2024, *ApJS*, 272, 2, doi: [10.3847/1538-4365/ad2b4d](https://doi.org/10.3847/1538-4365/ad2b4d)
- Li, M., Bryan, G. L., & Ostriker, J. P. 2017, *ApJ*, 841, 101, doi: [10.3847/1538-4357/aa7263](https://doi.org/10.3847/1538-4357/aa7263)
- Lian, J., Storm, N., Guiglion, G., et al. 2023, *MNRAS*, 525, 1329, doi: [10.1093/mnras/stad2390](https://doi.org/10.1093/mnras/stad2390)
- Lian, J., Thomas, D., Maraston, C., et al. 2020, *MNRAS*, 497, 2371, doi: [10.1093/mnras/staa2078](https://doi.org/10.1093/mnras/staa2078)
- Lian, J., Zasowski, G., Hasselquist, S., et al. 2022, *MNRAS*, 511, 5639, doi: [10.1093/mnras/stac479](https://doi.org/10.1093/mnras/stac479)
- Liu, S., Du, C., Newberg, H. J., et al. 2018, *ApJ*, 862, 163, doi: [10.3847/1538-4357/aac91](https://doi.org/10.3847/1538-4357/aac91)
- Loebman, S. R., Debattista, V. P., Nidever, D. L., et al. 2016, *ApJL*, 818, L6, doi: [10.3847/2041-8205/818/L6](https://doi.org/10.3847/2041-8205/818/L6)
- Looser, T. J., D'Eugenio, F., Maiolino, R., et al. 2023, arXiv e-prints, arXiv:2306.02470, doi: [10.48550/arXiv.2306.02470](https://doi.org/10.48550/arXiv.2306.02470)
- Looser, T. J., D'Eugenio, F., Arribas, S., et al. 2024, OASIS: Observing All phases of Stochastic Star formation - A census of galaxies at $z = 5.78$ over the entire SFR?M? plane, JWST Proposal. Cycle 3, ID. #5997
- Majewski, S. R., Schiavon, R. P., Frinchaboy, P. M., et al. 2017, *AJ*, 154, 94, doi: [10.3847/1538-3881/aa784d](https://doi.org/10.3847/1538-3881/aa784d)
- Maoz, D., Mannucci, F., & Brandt, T. D. 2012, *MNRAS*, 426, 3282, doi: [10.1111/j.1365-2966.2012.21871.x](https://doi.org/10.1111/j.1365-2966.2012.21871.x)
- Mardini, M. K., Frebel, A., Chiti, A., et al. 2022, *ApJ*, 936, 78, doi: [10.3847/1538-4357/ac8102](https://doi.org/10.3847/1538-4357/ac8102)
- Marinacci, F., Pakmor, R., & Springel, V. 2014, *MNRAS*, 437, 1750, doi: [10.1093/mnras/stt2003](https://doi.org/10.1093/mnras/stt2003)
- Meisner, A. M., Lang, D., Schlafly, E. F., & Schlegel, D. J. 2021, *Research Notes of the American Astronomical Society*, 5, 200, doi: [10.3847/2515-5172/ac21ca](https://doi.org/10.3847/2515-5172/ac21ca)
- Minchev, I., Chiappini, C., & Martig, M. 2013, *A&A*, 558, A9, doi: [10.1051/0004-6361/201220189](https://doi.org/10.1051/0004-6361/201220189)
- Minchev, I., Famaey, B., Quillen, A. C., et al. 2012, *A&A*, 548, A127, doi: [10.1051/0004-6361/201219714](https://doi.org/10.1051/0004-6361/201219714)
- Monachesi, A., Gómez, F. A., Grand, R. J. J., et al. 2019, *MNRAS*, 485, 2589, doi: [10.1093/mnras/stz538](https://doi.org/10.1093/mnras/stz538)
- Mori, A., Di Matteo, P., Salvadori, S., et al. 2024, arXiv e-prints, arXiv:2401.13737, doi: [10.48550/arXiv.2401.13737](https://doi.org/10.48550/arXiv.2401.13737)
- Muratov, A. L., Kereš, D., Faucher-Giguère, C.-A., et al. 2015, *MNRAS*, 454, 2691, doi: [10.1093/mnras/stv2126](https://doi.org/10.1093/mnras/stv2126)
- Naidu, R. P., Conroy, C., Bonaca, A., et al. 2020, *ApJ*, 901, 48, doi: [10.3847/1538-4357/abaef4](https://doi.org/10.3847/1538-4357/abaef4)
- Ness, M., & Freeman, K. 2016, *PASA*, 33, e022, doi: [10.1017/pasa.2015.51](https://doi.org/10.1017/pasa.2015.51)
- Nomoto, K., Kobayashi, C., & Tominaga, N. 2013, *ARA&A*, 51, 457, doi: [10.1146/annurev-astro-082812-140956](https://doi.org/10.1146/annurev-astro-082812-140956)
- Ojima, T., Ishimaru, Y., Wanajo, S., Prantzos, N., & François, P. 2018, *ApJ*, 865, 87, doi: [10.3847/1538-4357/aada11](https://doi.org/10.3847/1538-4357/aada11)
- Orkney, M. D. A., Laporte, C. F. P., Grand, R. J. J., et al. 2022, *MNRAS*, 517, L138, doi: [10.1093/mnrasl/slac126](https://doi.org/10.1093/mnrasl/slac126)
- . 2023, *MNRAS*, 525, 683, doi: [10.1093/mnras/stad2361](https://doi.org/10.1093/mnras/stad2361)
- Pallottini, A., & Ferrara, A. 2023, *A&A*, 677, L4, doi: [10.1051/0004-6361/202347384](https://doi.org/10.1051/0004-6361/202347384)
- Perryman, M. A. C., de Boer, K. S., Gilmore, G., et al. 2001, *A&A*, 369, 339, doi: [10.1051/0004-6361:20010085](https://doi.org/10.1051/0004-6361:20010085)
- Pinna, F., Walo-Martín, D., Grand, R. J. J., et al. 2024, *A&A*, 683, A236, doi: [10.1051/0004-6361/202347388](https://doi.org/10.1051/0004-6361/202347388)
- Planck Collaboration, Ade, P. A. R., Aghanim, N., et al. 2014, *A&A*, 571, A16, doi: [10.1051/0004-6361/201321591](https://doi.org/10.1051/0004-6361/201321591)
- Prantzos, N., Abia, C., Limongi, M., Chieffi, A., & Cristallo, S. 2018, *MNRAS*, 476, 3432, doi: [10.1093/mnras/sty316](https://doi.org/10.1093/mnras/sty316)
- Renaud, F., Agertz, O., Read, J. I., et al. 2021, *MNRAS*, 503, 5846, doi: [10.1093/mnras/stab250](https://doi.org/10.1093/mnras/stab250)
- Richter, P., Nuza, S. E., Fox, A. J., et al. 2017, *A&A*, 607, A48, doi: [10.1051/0004-6361/201630081](https://doi.org/10.1051/0004-6361/201630081)
- Rix, H.-W., Chandra, V., Andrae, R., et al. 2022, *ApJ*, 941, 45, doi: [10.3847/1538-4357/ac9e01](https://doi.org/10.3847/1538-4357/ac9e01)
- Santistevan, I. B., Wetzel, A., El-Badry, K., et al. 2020, *MNRAS*, 497, 747, doi: [10.1093/mnras/staa1923](https://doi.org/10.1093/mnras/staa1923)
- Schlesinger, K. J., Johnson, J. A., Rockosi, C. M., et al. 2012, *ApJ*, 761, 160, doi: [10.1088/0004-637X/761/2/160](https://doi.org/10.1088/0004-637X/761/2/160)
- Schmidt, M. 1959, *ApJ*, 129, 243, doi: [10.1086/146614](https://doi.org/10.1086/146614)

- Schneider, E. E., & Robertson, B. E. 2018, *ApJ*, 860, 135, doi: [10.3847/1538-4357/aac329](https://doi.org/10.3847/1538-4357/aac329)
- Schönrich, R., & Binney, J. 2009, *MNRAS*, 396, 203, doi: [10.1111/j.1365-2966.2009.14750.x](https://doi.org/10.1111/j.1365-2966.2009.14750.x)
- Skrutskie, M. F., Cutri, R. M., Stiening, R., et al. 2006, *AJ*, 131, 1163, doi: [10.1086/498708](https://doi.org/10.1086/498708)
- Sparre, M., Hayward, C. C., Feldmann, R., et al. 2017, *MNRAS*, 466, 88, doi: [10.1093/mnras/stw3011](https://doi.org/10.1093/mnras/stw3011)
- Spitoni, E., Cescutti, G., Minchev, I., et al. 2019, *A&A*, 628, A38, doi: [10.1051/0004-6361/201834665](https://doi.org/10.1051/0004-6361/201834665)
- Spitoni, E., Verma, K., Silva Aguirre, V., et al. 2021, *A&A*, 647, A73, doi: [10.1051/0004-6361/202039864](https://doi.org/10.1051/0004-6361/202039864)
- Stern, J., Faucher-Giguère, C.-A., Fielding, D., et al. 2021, *ApJ*, 911, 88, doi: [10.3847/1538-4357/abd776](https://doi.org/10.3847/1538-4357/abd776)
- Stevens, A. R. H., Lagos, C. d. P., Contreras, S., et al. 2017, *MNRAS*, 467, 2066, doi: [10.1093/mnras/stx243](https://doi.org/10.1093/mnras/stx243)
- Sun, G., Faucher-Giguère, C.-A., Hayward, C. C., et al. 2023, *ApJL*, 955, L35, doi: [10.3847/2041-8213/acf85a](https://doi.org/10.3847/2041-8213/acf85a)
- Tian, H., Liu, C., Xu, Y., & Xue, X. 2019, *ApJ*, 871, 184, doi: [10.3847/1538-4357/aaf6e8](https://doi.org/10.3847/1538-4357/aaf6e8)
- Ting, Y.-S. 2024, arXiv e-prints, arXiv:2412.05806, doi: [10.48550/arXiv.2412.05806](https://doi.org/10.48550/arXiv.2412.05806)
- Ting, Y.-S., Conroy, C., Rix, H.-W., & Cargile, P. 2019, *ApJ*, 879, 69, doi: [10.3847/1538-4357/ab2331](https://doi.org/10.3847/1538-4357/ab2331)
- Ting, Y.-S., & Ji, A. P. 2024, arXiv e-prints, arXiv:2408.06807, doi: [10.48550/arXiv.2408.06807](https://doi.org/10.48550/arXiv.2408.06807)
- van den Bergh, S. 1962, *AJ*, 67, 486, doi: [10.1086/108757](https://doi.org/10.1086/108757)
- Vera-Ciro, C., D'Onghia, E., & Navarro, J. F. 2016, *ApJ*, 833, 42, doi: [10.3847/1538-4357/833/1/42](https://doi.org/10.3847/1538-4357/833/1/42)
- Viswanathan, A., Horta, D., Price-Whelan, A. M., & Starkenburg, E. 2024, arXiv e-prints, arXiv:2411.12165, doi: [10.48550/arXiv.2411.12165](https://doi.org/10.48550/arXiv.2411.12165)
- Vogelsberger, M., Genel, S., Sijacki, D., et al. 2013, *MNRAS*, 436, 3031, doi: [10.1093/mnras/stt1789](https://doi.org/10.1093/mnras/stt1789)
- Wagoner, R. V., Fowler, W. A., & Hoyle, F. 1967, *ApJ*, 148, 3, doi: [10.1086/149126](https://doi.org/10.1086/149126)
- Weinberg, D. H., Holtzman, J. A., Hasselquist, S., et al. 2019, *ApJ*, 874, 102, doi: [10.3847/1538-4357/ab07c7](https://doi.org/10.3847/1538-4357/ab07c7)
- Xiang, M., Rix, H.-W., Yang, H., et al. 2024, *Nature Astronomy*, doi: [10.1038/s41550-024-02382-w](https://doi.org/10.1038/s41550-024-02382-w)
- Xiang, M., Rix, H.-W., Ting, Y.-S., et al. 2022, *A&A*, 662, A66, doi: [10.1051/0004-6361/202141570](https://doi.org/10.1051/0004-6361/202141570)
- Xylakis-Dornbusch, T., Christlieb, N., Hansen, T. T., et al. 2024, *A&A*, 687, A177, doi: [10.1051/0004-6361/202348885](https://doi.org/10.1051/0004-6361/202348885)
- Xylakis-Dornbusch, T., Christlieb, N., Lind, K., & Nordlander, T. 2022, *A&A*, 666, A58, doi: [10.1051/0004-6361/202243811](https://doi.org/10.1051/0004-6361/202243811)
- Yanny, B., Rockosi, C., Newberg, H. J., et al. 2009, *AJ*, 137, 4377, doi: [10.1088/0004-6256/137/5/4377](https://doi.org/10.1088/0004-6256/137/5/4377)
- Yao, Y., Ji, A. P., Kuposov, S. E., & Limberg, G. 2024, *MNRAS*, 527, 10937, doi: [10.1093/mnras/stad3775](https://doi.org/10.1093/mnras/stad3775)
- Ye, X., Wu, W., Allende Prieto, C., et al. 2024, arXiv e-prints, arXiv:2411.19105, doi: [10.48550/arXiv.2411.19105](https://doi.org/10.48550/arXiv.2411.19105)
- Youakim, K., Starkenburg, E., Martin, N. F., et al. 2020, *MNRAS*, 492, 4986, doi: [10.1093/mnras/stz3619](https://doi.org/10.1093/mnras/stz3619)
- Zhang, H., Zaritsky, D., Olsen, K. P., et al. 2021, *ApJ*, 916, 101, doi: [10.3847/1538-4357/ac0433](https://doi.org/10.3847/1538-4357/ac0433)
- Zhang, X., Green, G. M., & Rix, H.-W. 2023, *MNRAS*, 524, 1855, doi: [10.1093/mnras/stad1941](https://doi.org/10.1093/mnras/stad1941)
- Zhao, G., Zhao, Y.-H., Chu, Y.-Q., Jing, Y.-P., & Deng, L.-C. 2012, *Research in Astronomy and Astrophysics*, 12, 723, doi: [10.1088/1674-4527/12/7/002](https://doi.org/10.1088/1674-4527/12/7/002)